

# A deep radius valley revealed by *Kepler* short cadence observations

Cynthia S. K. Ho   and Vincent Van Eylen 

*Mullard Space Science Laboratory, University College London, Dorking RH5 6NT, UK*

Accepted 2022 December 19. Received 2022 December 2; in original form 2022 October 17

## ABSTRACT

The characteristics of the radius valley, i.e. an observed lack of planets between 1.5 and 2 Earth radii at periods shorter than about 100 d, provide insights into the formation and evolution of close-in planets. We present a novel view of the radius valley by refitting the transits of 431 planets using *Kepler* 1-min short cadence observations, the vast majority of which have not been previously analysed in this way. In some cases, the updated planetary parameters differ significantly from previous studies, resulting in a deeper radius valley than previously observed. This suggests that planets are likely to have a more homogeneous core composition at formation. Furthermore, using support vector machines, we find that the radius valley location strongly depends on orbital period and stellar mass and weakly depends on stellar age, with  $\partial \log(R_{p,\text{valley}})/\partial \log P = -0.096^{+0.023}_{-0.027}$ ,  $\partial \log(R_{p,\text{valley}})/\partial \log M_{\star} = 0.231^{+0.053}_{-0.064}$ , and  $\partial \log(R_{p,\text{valley}})/\partial \log(\text{age}) = 0.033^{+0.017}_{-0.025}$ . These findings favour thermally driven mass-loss models such as photoevaporation and core-powered mass-loss, with a slight preference for the latter scenario. Finally, this work highlights the value of transit observations with a short photometric cadence to precisely determine planet radii, and we provide an updated list of precisely and homogeneously determined parameters for the planets in our sample.

**Key words:** planets and satellites: composition – planets and satellites: formation – planets and satellites: fundamental parameters.

## 1 INTRODUCTION

The ‘radius valley’, also known as the ‘radius gap’, is the relative paucity of planets with sizes between about 1.5 and 2 Earth radii at orbital periods less than about 100 d. This phenomenon has been predicted theoretically due to the heavy radiation these close-in planets receive from their host star (e.g. Lopez & Fortney 2013; Owen & Wu 2013) and was subsequently seen observationally (e.g. Fulton et al. 2017; Fulton & Petigura 2018; Van Eylen et al. 2018). Several theories have been suggested to explain the physical origin of the radius valley. On one hand, thermally driven mass-loss scenarios have been proposed, which include photoevaporation (e.g. Lopez & Fortney 2013; Owen & Wu 2013; Owen & Wu 2017) and core-powered mass-loss (e.g. Ginzburg, Schlichting & Sari 2018; Gupta & Schlichting 2019, 2020) models. In these scenarios, the valley separates planets that have lost their atmosphere from those that have retained it. Alternatively, late gas-poor formation, where planets below the valley have formed atmosphere-free, may also be able to explain the origin of the valley (e.g. Lee, Chiang & Ormel 2014; Lee & Chiang 2016; Lopez & Rice 2018; Cloutier & Menou 2020).

Observed characteristics of the radius valley can therefore reveal the properties of these close-in planets and their formation history. For example, in photoevaporation models, the location of the radius valley and its slope as a function of orbital period depend on the planetary composition and photoevaporation physics (Owen & Wu 2017; Mordasini 2020). The valley’s location and relative emptiness can therefore be used to infer the composition of planets surrounding

it and their relative homogeneity (e.g. Van Eylen et al. 2018). Planets located inside the radius valley may have a different composition or could be undergoing the final stages of atmospheric loss by thermally driven mechanisms and hence may be important targets for further studies (e.g. Owen & Wu 2017; Gupta & Schlichting 2019; Petigura 2020). The valley’s location as a function of orbital period can be used to distinguish between thermal mass-loss models, which exhibit a negative slope as a function of orbital period, and late gas-poor formation models, which have the opposite slope (e.g. Van Eylen et al. 2019; Cloutier & Menou 2020; Van Eylen et al. 2021). Within thermal mass-loss models, photoevaporation and core-powered mass-loss models predict a different dependence of the valley’s location on stellar mass and age (e.g. Rogers et al. 2021).

Observationally, these valley characteristics have been challenging to reliably ascertain. A deficit of planets with sizes around 1.5–2 Earth radii ( $R_{\oplus}$ ) was first observed by Fulton et al. (2017) in a sample of 2025 planets, with stellar radii determined spectroscopically as part of the California-*Kepler* survey (CKS). These planets were about a factor of 2 rarer than planets both smaller and larger. Independently, Van Eylen et al. (2018, hereafter V18) analysed a subset of this sample (117 planets), incorporating higher-precision stellar parameters using asteroseismology and refitting transit light curves to achieve a median uncertainty on planet sizes of 3.3 per cent. This study revealed the valley’s slope as a function of orbital period for the first time, and suggested the radius valley may be very deep or even entirely empty. The tension between the valley’s views of Fulton et al. (2017) and V18 was further exacerbated when the precision of stellar parameters of the former study were further improved by Fulton & Petigura (2018, hereafter F18). Despite improving stellar uncertainties from 11 to 3 per cent by incorporating Gaia

\* E-mail: [sze.ho.20@ucl.ac.uk](mailto:sze.ho.20@ucl.ac.uk)

parallaxes, the valley remained partially filled in, with its depth largely unchanged.

Petigura (2020) investigated the discrepancy in the valley’s depth between V18 and F18 and concluded it is unlikely to be caused by differing sample sizes or differing values or uncertainties in stellar radii. The study argued that the 6.9 per cent dispersion in planetary radii is instead primarily caused by a discrepancy in the ratio of planet to stellar radii ( $R_p/R_*$ ) determined from the transit fits. F18 used radius ratios from Mullally et al. (2015), which fitted *Kepler* 30-min ‘long cadence’ observations, whereas V18 used *Kepler* 1-min ‘short cadence’ observations, also used for orbital eccentricity determination and described in Van Eylen & Albrecht (2015) and Van Eylen et al. (2019).

Here, we seek to refit planet transits for the full subset of F18 for which short cadence observations are available. This increases the sample of planets relevant for the radius valley for which short cadence transit fits are used from 60 in V18 to 431 here. Furthermore, we will apply the methods to determine the valley’s location and slope used by V18, notably the use of support vector machines (SVMs), to this larger sample, and we expand to other dimensions such as stellar mass and age.

In Section 2, we describe the sample and methodology used to analyse the radius valley. In Section 3, we present the results of this analysis, such as revised planetary sizes, the depth of the valley, and its dependence on parameters such as the orbital period and stellar mass and age. These findings are compared to other observational studies and theoretical models in Section 4. Finally, we provide conclusions in Section 5.

## 2 METHODS

### 2.1 Sample selection

We use the sample of planets for which stellar parameters are available from F18 as a starting point. To focus on the radius valley, we limit the sample to planets with radii  $1 \leq R_p/R_\oplus \leq 4$  and orbital periods  $1 \leq P/\text{days} \leq 100$ , resulting in a sample of 1272 planets (for comparison, applying the same period and radius cuts to the sample studied by V18 leaves 74 planets). As *Kepler* 1-min short cadence observations may yield superior precision (Petigura 2020), we further limit our sample to those planets for which at least 6 months of *Kepler* short cadence data are available.

To avoid issues with transit fitting related to transit timing variations (TTVs), we also remove planets with known TTVs based on the catalogue by Holczer et al. (2016). We further exclude KOI-1576.03, as we find that the short cadence data suggested an orbital period different to the one recorded in the archive. Furthermore, we exclude any planets that are classified as potential false positives in Petigura et al. (2017). The results in a total sample size of 431 planets, 60 of which have parameters previously analysed by V18 and 371 which have not (a further 14 planets in V18 have TTVs and are not reanalysed here).

### 2.2 Data reduction

The 1-min *Kepler* short cadence Pre-search Data Conditioning SAP (Stumpe et al. 2012; Smith et al. 2012) light curves of these targets are downloaded from the NASA *Mikulski Archive for Space Telescopes* (MAST) database using the `lightkurve` package (Lightkurve Collaboration et al. 2018), which incorporates `astroquery` (Ginsburg et al. 2019) and `astropy` (Astropy Collaboration et al. 2013, 2018) dependencies. We only retain data within 0.2 d before the estimated

ingress and after the estimated egress of the transits of the planets of interest, using the transit durations and mid-times in Mullally et al. (2015) as the expected transit locations. For multiplanet systems, we only retain transits of planets that are within our sample. We remove data outliers that lie beyond  $6\sigma$  from the median after masking the transits. We then flatten the transits by dividing the data points with the slope obtained by performing linear regression on the data points immediately before ingress and after egress, to remove long-term systematic trends present in the transits. We then again remove data outliers with  $\sigma = 5$  to further clean the data.

### 2.3 Stellar multiplicity

Around 46 per cent of solar-type stars have at least one stellar companion (Raghavan et al. 2010). When a planet orbits a single star, the transit depth  $\delta$  is approximately given by

$$\delta = \frac{\Delta F}{F_{\text{tot}}} \approx \frac{R_p^2}{R_*^2}, \quad (1)$$

where  $F_{\text{tot}}$  is the total stellar flux,  $\Delta F$  is the change in stellar flux, and  $R_p$  and  $R_*$  are the planetary and stellar radius, respectively. However, in a multistellar system, the total flux is the sum of fluxes of all stars in the system, but the change in flux during transit is only relative to the star(s) which the planet transits (Furlan et al. 2017). Therefore, it is important to take into account the effect of nearby stars on the light curve flux.

Furlan et al. (2017) compiled a catalogue of *Kepler* Objects of Interest (KOI) observations with adaptive optics, speckle interferometry, lucky imaging, and imaging from space with the Hubble Space Telescope. The typical point spread function widths and sensitivities ( $\Delta m$ ) are different for every observation method, target and bandpass; hence, whether stellar companions are detected is dependent on the above factors. For example, Furlan et al. (2017) were able to detect a median  $\Delta m \sim 8$  mag with Keck in the *K* band at a separation of  $\sim 0.5$  arcsec, but only at  $\sim 2.5$  arcsec at Lick in the *J* or *H* bands. About 30 per cent of KOIs observed in Furlan et al. (2017) have at least one companion detected within 4 arcsec (Furlan et al. 2017), and given a mean distance of 616 pc for the 431 planets in our sample computed from distances reported in Mathur et al. (2017), corresponds to  $\sim 2464$  au.

Here, we adopt the ‘radius correction factor’ (RCF), given in Furlan et al. (2017) as

$$\text{RCF} = \frac{R_{p,\text{corr}}}{R_{p,\text{uncorr}}} \quad (2)$$

and multiply the normalized *Kepler* light curve fluxes by  $\text{RCF}^2$ , and subtract  $(\text{RCF}^2 - 1)$  to re-normalize, to obtain the corrected light curve reflecting the transit of one planet orbiting around one star. In total, 137 of the 431 planets in our sample (32 per cent) have RCF measurements from Furlan et al. (2017).

### 2.4 Transit fitting

We use the `exoplanet` package (Foreman-Mackey et al. 2021) to generate a transit light curve model with quadratic stellar limb darkening, and then run a Hamiltonian Monte Carlo (HMC) algorithm implemented in `PyMC3` (Salvatier, Wiecki & Fonnesbeck 2016) to perform fitting and determine orbital parameter posteriors. We also implement a Gaussian process (GP) model (Rasmussen & Williams 2006) to account for correlated noise in the light curves. However, for *Kepler*-65 and *Kepler*-21 A, we do not fit for a GP model due to convergence constraints. The parameters fitted for each

**Table 1.** Table showing estimates of the orbital periods ( $P$ ), planetary-to-stellar-radii ratio ( $R_p/R_*$ ), planetary radii ( $R_p$ ), the number of transits in the fitted light curve ( $N_{tr}$ ) of 431 planets refitted in this work. The source of  $R_*$  to convert  $R_p/R_*$  to  $R_p$  is listed in the references column: (1) F18, (2) V18. ‘Flag’ refers to whether the planet passes the filter checks and is included in the smaller subset for further analyses (1 for true and 0 for false). The complete list of parameters is provided in Appendix A. Only the first 10 planets are shown here; the full table is available online in a machine-readable format.

KOI	Kepler name	$P$ (d)	$R_p/R_*$	$R_p$ ( $R_\oplus$ )	$R_*$ source	$N_{tr}$	Flag
K00041.01	Kepler-100 c	$12.815\,893 \pm 0.000\,008$	$0.0138 \pm 0.0002$	$2.28^{+0.03}_{-0.03}$	(2)	93	1
K00041.02	Kepler-100 b	$6.887\,062 \pm 0.000\,007$	$0.0082 \pm 0.0001$	$1.36^{+0.03}_{-0.03}$	(2)	173	1
K00041.03	Kepler-100 d	$35.333\,093 \pm 0.000\,019$	$0.0104 \pm 0.0002$	$1.71^{+0.04}_{-0.04}$	(2)	35	1
K00046.02	Kepler-101 c	$6.029\,792 \pm 0.000\,020$	$0.0073 \pm 0.0007$	$1.32^{+0.14}_{-0.14}$	(1)	50	0
K00049.01	Kepler-461 b	$8.313\,784 \pm 0.000\,015$	$0.0287 \pm 0.0010$	$4.03^{+0.17}_{-0.17}$	(1)	34	1
K00069.01	Kepler-93 b	$4.726\,739 \pm 0.000\,001$	$0.0151 \pm 0.0001$	$1.50^{+0.04}_{-0.04}$	(2)	275	1
K00070.01	Kepler-20 A c	$10.854\,089 \pm 0.000\,003$	$0.0290 \pm 0.0002$	$2.79^{+0.07}_{-0.07}$	(1)	116	1
K00070.02	Kepler-20 A b	$3.696\,115 \pm 0.000\,001$	$0.0182 \pm 0.0002$	$1.75^{+0.05}_{-0.04}$	(1)	336	1
K00070.03	Kepler-20 A d	$77.611\,598 \pm 0.000\,019$	$0.0263 \pm 0.0003$	$2.52^{+0.07}_{-0.07}$	(1)	15	1
K00070.05	Kepler-20 A f	$19.577\,627 \pm 0.000\,020$	$0.0091 \pm 0.0004$	$0.88^{+0.04}_{-0.04}$	(1)	62	1
...	...	...	...	...	...	...	...

planet are orbital period ( $P$ ), transit mid-time ( $t_0$ ), ratio between planetary and stellar radii ( $R_p/R_*$ ), impact parameter ( $b$ ), eccentricity ( $e$ ), argument of periastris ( $\omega$ ), and stellar density ( $\rho_*$ ). For each light curve, we further include two quadratic stellar limb darkening parameters ( $u_0$  and  $u_1$ ) for the host star, with bounds  $0 < u_0, u_1 < 1$  and implemented with the Kipping (2013) reparameterization in `exoplanet`, the transit jitter ( $\sigma_{ic}$ ), and two parameters describing the GP contribution ( $\sigma_{gp}$ ,  $\rho_{gp}$ ).

We initialize the HMC chains by using values presented in the *Kepler* Q1-16 data set (Mullally et al. 2015) for  $P$ ,  $t_0$ ,  $R_p/R_*$ , and  $b$ . We set the system to begin with near-circular orbits, with  $e = 0.01$  and  $\omega = 0.01$  rad. We take initial stellar densities from F18. We use the Exoplanet Characterization ToolKit (Bourque et al. 2021) to estimate the initial  $u_0$  and  $u_1$ , which takes the stellar temperature, surface gravity, and metallicity, which we use values from the *Kepler* Q1-16 data set (Mullally et al. 2015), as inputs.

We apply Gaussian priors to  $P$ ,  $t_0$ ,  $u_0$ ,  $u_1$ , and  $\rho_*$ , using the initial guesses as the mean, and  $\sigma_P = 2 \times 10^{-5}$  d,  $\sigma_{t_0} = 10^{-3}$  d,  $\sigma_{u_i} = 0.2$ , and the  $\rho_*$  uncertainty from F18 if available, and Mullally et al. (2015) otherwise. A beta distribution prior, according to Van Eylen et al. (2019), is placed on  $e$ , which is

$$\text{PDF}(e, \alpha, \beta) \propto e^\alpha (1 - e)^\beta \quad (3)$$

with  $\alpha = 1.58$  and  $\beta = 4.4$  for system with only one transiting planet, and  $\alpha = 1.52$  and  $\beta = 29$  for a multitransiting-planet system.

### 3 RESULTS

#### 3.1 Revised planet parameters

We report the updated orbital periods ( $P$ ), planetary-to-stellar-radii ratio ( $R_p/R_*$ ), planetary radii ( $R_p$ ), the number of transits in the fitted light curve ( $N_{tr}$ ), and their uncertainties of the 431 planets fitted in this sample in Table 1. The full list of parameters are provided in Appendix A. We convert our  $R_p/R_*$  to  $R_p$  using the updated stellar parameters available: values used in V18 from asteroseismology (i.e. taken from Huber et al. 2013; Silva Aguirre et al. 2015; Lundkvist et al. 2016) if the planets are included in the V18 samples, and F18 otherwise. Full homogeneity is lost by using stellar radii from two sources. To investigate the consequences of this, we compute the difference,  $\delta_{R_p}$ , between the planetary radii obtained by converting

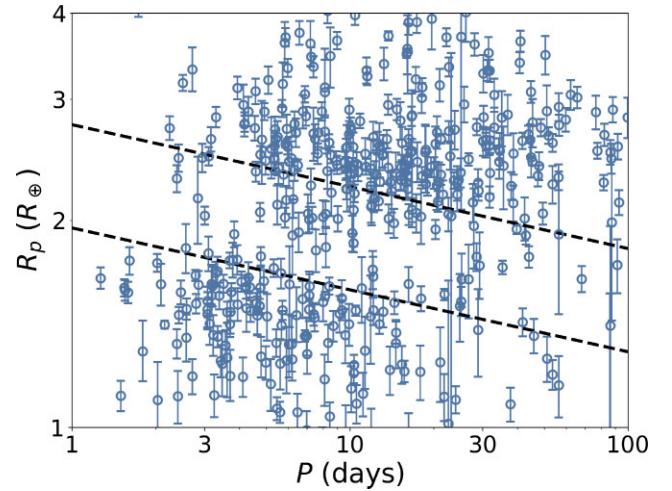


**Figure 1.** Radius–period plot of all 431 planets refitted in this work. The black-dotted lines indicate the upper and lower boundaries of the radius valley defined in V18.

$R_p/R_*$  to  $R_p$  using  $R_*$  from F18 and V18, and found the mean  $\delta$ ,  $\delta = 0.03 \pm 0.11$ ; hence,  $\delta = 0$  (no difference) is well within  $1\sigma$ , and we conclude that there is no substantial drawbacks of using multiple sources. This sample of 431 planets with updated parameters is plotted on the radius–orbital period plot as shown in Fig. 1.

We present the typical uncertainties of  $R_p/R_*$  and  $R_p$  of planets fitted in this work, compared with F18 and V18 in Table 2. For our newly fitted results, we find that  $R_p/R_*$  has a mean uncertainty of 4.76 per cent, and a median uncertainty of 3.44 per cent. This is smaller when compared to the mean and median uncertainties of 8.73 and 4.07 per cent, respectively, for the F18 sample. For  $R_p$ , we find a mean and median uncertainty of 6.09 and 4.70 per cent in our work, again smaller compared to 10.00 and 5.22 per cent for F18. However, they are larger than that of V18, possibly due to V18 analysing brighter stars, hence the light curves are less noisy. This can be seen by comparing the mean photometric flux error of the transit light curves fitted: 1007 parts per million (ppm) for this work, and 271 ppm for V18.

**Table 2.** Mean and median values radii determined in this work, F18, and V18. Values are listed as percentages (%).

Parameter		This work	F18	V18
Sample size		431	1901	117
$R_p/R_*$	Mean	4.76	8.73	3.20
	Median	3.44	4.07	2.44
$R_*$	Mean	3.23	3.17	2.49
	Median	2.78	2.74	2.20
$R_p$	Mean	6.09	10.00	3.96
	Median	4.70	5.22	3.36

We select the planets in F18 that are in common with the planets in our sample, and examine the change in  $R_p$ . We find that 217 planets have a larger  $R_p$  after refitting, and smaller for 214 planets. Of the planets whose sizes have increased, the mean change is 9.79 per cent, and 8.69 per cent for planets with reduced sizes. Considering all 431 planets, our new results change  $R_p$  by a mean and median of only 0.62 and 0.02 per cent, respectively, indicating that our refitting results do not systematically alter the planet sizes. We observe that 120 planets (28 per cent) have a revised  $R_p > 2\sigma$  away from their corresponding values from F18, and 62 planets (14 per cent)  $> 3\sigma$  away.

### 3.2 Radius valley dependence on orbital period

To obtain the most precise planetary sample, we apply the following conservative cuts to our sample for subsequent analyses in the rest of this paper:

- (i) *Precision on  $R_p$* : We exclude planets with a planet radius precision  $\sigma_{R_p} > 10$  per cent.
- (ii) *Radius correction factor (RCF)*: We exclude planets with an RCF  $> 5$  per cent, as reported in Furlan et al. (2017). RCFs may themselves be uncertain due to observational challenges in detecting nearby stellar companions and measuring their brightness (Furlan et al. 2017). Of the 137 planets with RCF measurements from Furlan et al. (2017), 18 (13 per cent) have RCF  $> 5$  per cent. The remaining 294 planets do not have RCF measurements currently available.
- (iii) *Number of transits*: We exclude planets with fewer than three transits in the *Kepler* short cadence data to limit the risk that correlated noise during an individual transit strongly affects the resulting fit.

After implementing these filters, 375 planets remain in our sample which we will use throughout the remainder of this work.

We first use this sample to investigate the location of the radius valley as a function of orbital period. Following the procedure outlined in V18, we calculate the position of the radius valley by determining the hyperplane of maximum separation. We perform this with a linear SVM. To initialize our model, we initially classify our sample into two groups, ‘above’ and ‘below’ the radius valley on the radius-orbital period plane, by applying a Gaussian mixture model with two components in the  $R_p$ – $P$  plane. Since the orders of magnitude of  $R_p$  and  $P$  are different, we divide  $P$  by 5 before applying the above clustering algorithm to allow the model to separate the planetary population into two groups above and below the radius valley. Otherwise, the population would be clustered in a way dominated by the difference in period. Following V18 and David et al. (2021), we select an SVM penalty parameter of  $C = 10$  for the hyperplane, to minimize misclassification of data points above or below the radius valley, but still allow the hyperplane location to

be determined by a sufficient number of data points. To determine accurate uncertainties on the location of the valley, we then perform a bootstrap by generating 1000 new sample sets on which we repeat the above procedure. Each bootstrap sample is generated by generating a new sample of the same size from the original sample, allowing replacement. Each bootstrapped sample is then categorized into two groups with a Gaussian mixture model, and the SVM procedure is repeated. Reporting the median value and taking the 16th and 84th percentiles as the upper and lower uncertainties, we find

$$\log_{10} (R_p/R_{\oplus}) = m \log_{10} (P/\text{days}) + c \quad (4)$$

with  $m = -0.11 \pm 0.02$ , and  $c = 0.37^{+0.02}_{-0.03}$ . The location of the radius valley is plotted in Fig. 2.

We also implement the method adopted by Petigura et al. (2022), which involves computing the planet density in the radius-period plane with a Gaussian kernel density estimate (KDE), and fitting the planet radius at the KDE minima between  $\log_{10}(P/\text{days}) = 0.5 - 1.5$  (i.e.  $P \approx 3.16 - 31.6$  d) and  $\log_{10}(R_p/R_{\oplus}) = 0.15 - 0.35$  (i.e.  $R_p \approx 1.41 - 2.24 R_{\oplus}$ ) according to equation (4), and performing bootstrap with 1000 sample sets to find the uncertainties. The result is illustrated in Fig. 2. We use a KDE bandwidth of 0.467 in  $\log_{10}P$  and 0.075 in  $\log_{10}R_p$ , which is based on the bandwidth used by Petigura et al. (2022), but scaled up linearly based on the ratios between the two sample sizes. We note that this method fits a narrower period range compared to the SVM method, which fits for the full  $P = 1 - 100$  d. With this method, we obtain  $m = -0.12^{+0.03}_{-0.05}$  and  $c = 0.37^{+0.05}_{-0.03}$ . We find this value to be slightly steeper than that determined with the SVM, however, the two values are well within  $1\sigma$  of each other. Here, we do not correct for detection completeness, and we note that this method is highly sensitive to the choice of the KDE bandwidth, and using a bandwidth five times larger results with a slope approximately twice as steep.

Some studies have opted to study the radius valley location as a function of incident flux  $S$ , in addition to, or instead of,  $P$  (e.g. Rogers et al. 2021; Petigura et al. 2022). We calculate  $S$  according to the formula

$$S = \frac{L_{\star}}{4\pi a^2} \quad (5)$$

where  $L_{\star}$  is the host star’s luminosity.  $L_{\star}$  can itself be calculated using

$$L_{\star} = 4\pi R_{\star}^2 \sigma_{\text{sb}} T_{\text{eff}}^4 \quad (6)$$

where  $R_{\star}$  is the stellar radius,  $\sigma_{\text{sb}}$  is the Stefan–Boltzmann constant, and  $T_{\text{eff}}$  is the effective temperature of the star. Finally,  $a$  is the orbital semimajor axis, which is given by

$$\left(\frac{a}{R_{\star}}\right)^3 = \frac{GP^2\rho_{\star}(1+e\sin\omega)^3}{3\pi(1-e^2)^{1.5}} \quad (7)$$

according to Kepler’s third law of planetary motion (e.g. Van Eylen & Albrecht 2015; Petigura 2020). Here,  $G$  is the gravitational constant,  $P$  is the orbital period,  $\rho_{\star}$  is the stellar density,  $e$  and  $\omega$  are the orbital eccentricity and argument of periapsis, respectively. As before, we obtain the stellar properties ( $R_{\star}$ ,  $\rho_{\star}$ ,  $T_{\text{eff}}$ ) from V18 when available, and from F18 otherwise.  $P$ ,  $e$ , and  $\omega$  are obtained from the transit fitting results of this work. Fitting the valley with the SVM, we obtain

$$\log_{10} R_p/R_{\oplus} = m \log_{10} S/S_{\oplus} + c \quad (8)$$

with  $m = 0.07^{+0.02}_{-0.01}$ , and  $c = 0.11^{+0.03}_{-0.04}$ . The location of the radius valley in terms of  $S$  is shown in Fig. 3.

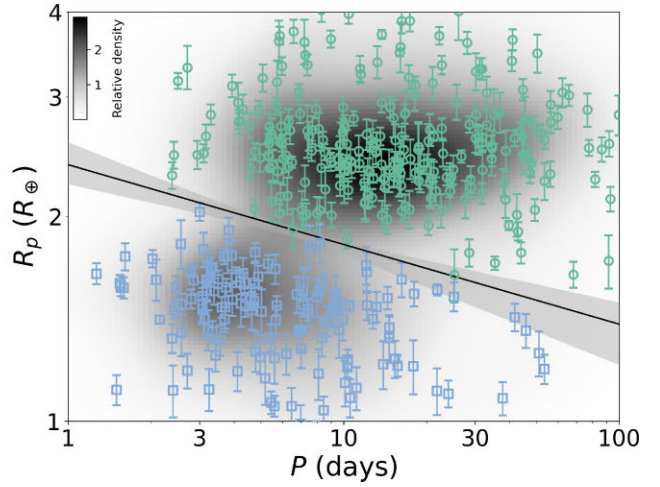
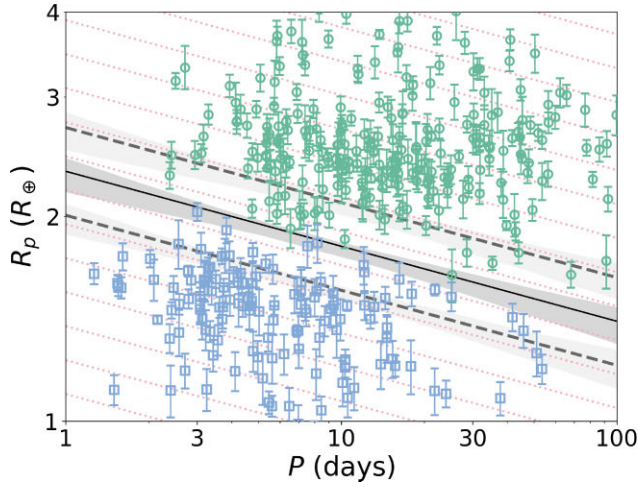


**Figure 2.** Left-hand panel: Radius valley location determined with the SVM, with  $m = -0.11 \pm 0.02$ , and  $c = 0.36^{+0.02}_{-0.03}$ , indicated by the black solid line. The dashed lines represent the median boundaries passing through the supporting vectors determining the position of the solid line. We define the area between the two lines as the radius valley region. The green and blue points show planets above and below the radius valley, respectively. The grey-shaded regions represent the  $\pm 1\sigma$  uncertainties of the lines determined using the bootstrap method. The red-dotted lines show the plot divided into multiple orbital-period dependent bins, which is then used for plotting the adjusted histogram in Fig. 4. Right-hand panel: radius valley position determined by fitting a line through the region where the kernel density estimate is minimum. With this method, we obtain  $m = -0.12^{+0.03}_{-0.05}$ , and  $c = 0.37^{+0.0}_{-0.03}$ , indicated by the black solid line with  $\pm 1\sigma$  uncertainty shaded in grey.

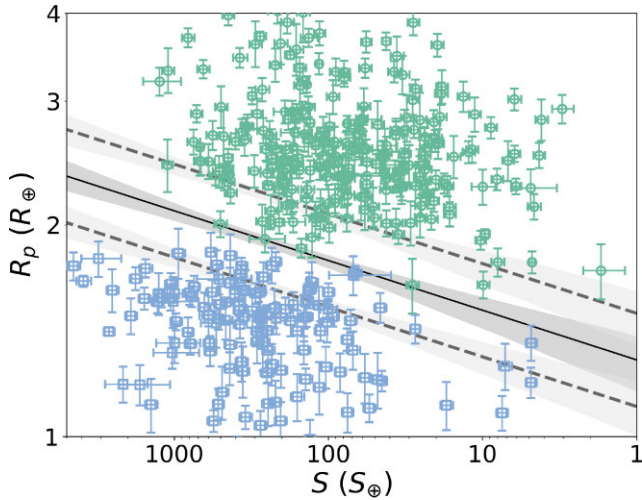


**Figure 3.** Same as Fig. 2 left-hand panel, but as a function of incident flux  $S$  instead of orbital period  $P$ .

### 3.3 Depth of the radius valley

We investigate the depth of the radius valley. As we find the position of the radius valley is dependent on the orbital period, we divide the radius valley into multiple tilted bins (as shown in Fig. 2 left-hand panel) and plot an adjusted histogram in logarithmic scale. We shift planets along the slope of the radius valley obtained with the SVM method in Section 3.2, i.e.  $m = -0.11$ , and plot a histogram of ‘expected’ planetary radii at an orbital period of 10 d, shown in Fig. 4. We choose to fit the histogram with a Gaussian mixture model of two clusters, as opposed to a Gaussian kernel density estimate, as the former is independent of the sizes and locations of the histogram bins, as well as the Gaussian bandwidth. Also, with the Gaussian mixture model, we are able to force the planets to fall into two groups only, matching the bimodal distribution of small planets.

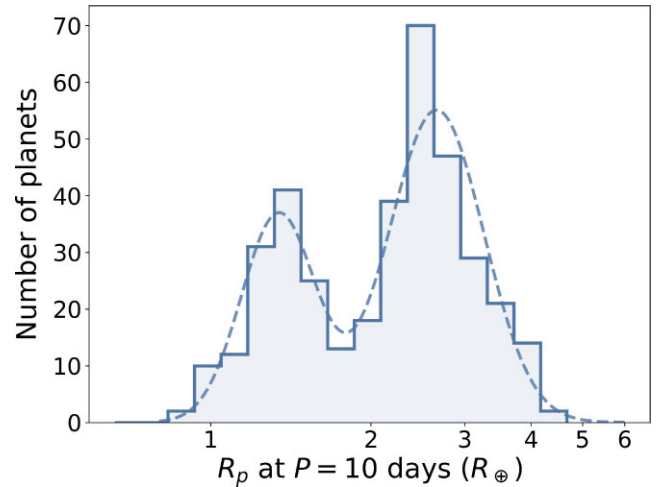


**Figure 4.** Histogram of planet radii, adjusted to equivalent radii at  $P = 10$  d, according to the radius valley slope calculated in Section 3.2 with the SVM. Note that completeness corrections are not performed. Here,  $E_{\text{avg}} = 2.98^{+0.60}_{-0.47}$ .

Here, we propose the metric  $E$ , defined as

$$E_{\text{SN}} = N_{\text{sub-Neptune, peak}} / N_{\text{valley}} \quad (9)$$

and

$$E_{\text{SE}} = N_{\text{super-Earth, peak}} / N_{\text{valley}} \quad (10)$$

to compare the number of planets inside the valley and the peak number outside the valley. A higher  $E$  indicates a deeper radius valley.  $N_{\text{sub-Neptune, peak}}$  and  $N_{\text{super-Earth, peak}}$  are the number of planets at the sub-Neptune and super-Earth Gaussian peaks respectively, and  $N_{\text{valley}}$  is the number of planets at the lowest point between the two Gaussian peaks. As  $N_{\text{sub-Neptune, peak}}$ ,  $N_{\text{super-Earth, peak}}$ , and  $N_{\text{valley}}$  are determined directly from the curve resulting from the Gaussian mixture model, this  $E$  metric is also independent of the

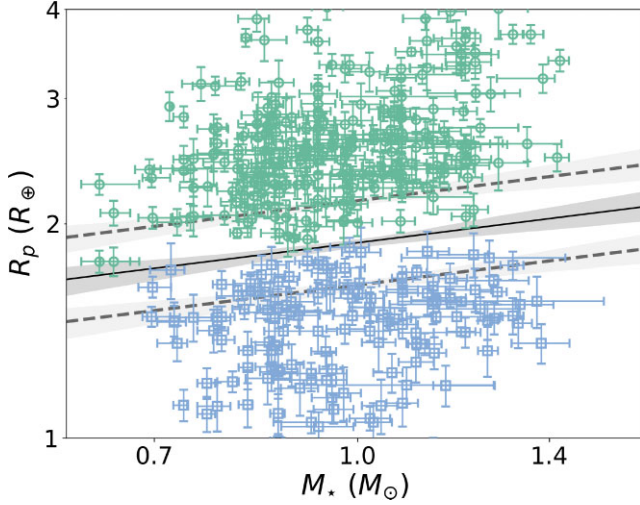
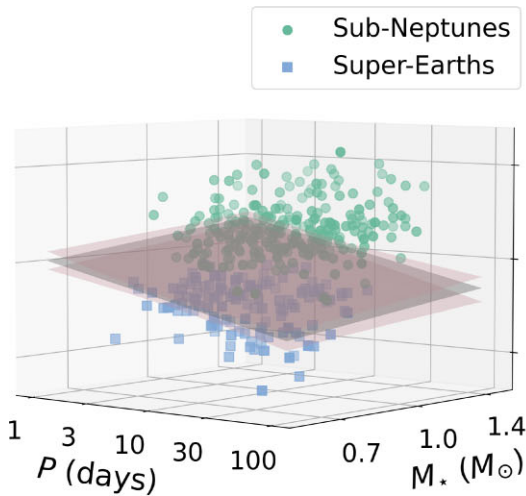


**Figure 5.** Plot of planetary radius against mass of host star. The solid line shows the location of the radius valley determined with the SVM, with slope  $m = 0.23^{+0.09}_{-0.08}$ , and  $c = 0.27 \pm 0.01$ . The dashed lines show the boundaries of the radius valley, given by the same  $m$ , and  $c_{\text{upper}} = 0.33 \pm 0.01$ ,  $c_{\text{lower}} = 0.22 \pm 0.01$ . The shaded regions depict the  $\pm 1\sigma$  uncertainties of the lines determined with bootstrapping.

histogram bin sizes or locations. To calculate the uncertainties of  $E$ , we again perform a bootstrap with 1000 sample sets, where each bootstrap sample is generated by generating a new sample of the same size from the original, allowing replacements. We also replace the radius of each selected planet by randomly drawing from a normal distribution with the reported planet radius as the mean, and the uncertainties on the radius as the variance. We report the median of this bootstrap distribution as our results, and the 84th and 16th percentiles as our  $\pm 1\sigma$  uncertainties. We test this metric on known planetary samples on F18 and V18, which we know the difference in the radius valley depth, and find that their corresponding  $E$  value differ, hence demonstrating the reliability of such metric. The difference in the depth of the radius valley is further discussed in Section 4.3. We find that for our new short cadence results, the



ratios are  $E_{\text{SN}} = 3.59^{+0.77}_{-0.62}$  and  $E_{\text{SE}} = 2.40^{+0.61}_{-0.41}$ . Averaging the two numbers gives us  $E_{\text{avg}} = 2.98^{+0.60}_{-0.47}$ .

### 3.4 Radius valley dependence on stellar mass

We investigate the radius valley location as a function of stellar mass. We first implement a two-dimensional SVM, using the same method as in Section 3.2. The result is shown in Fig. 5. We find  $d \log R_p / d \log M_* = 0.23^{+0.09}_{-0.08}$ , and the intercept  $c = 0.27 \pm 0.01$ .

Rogers et al. (2021) suggested the degeneracy between the photoevaporation and core-powered mass-loss scenarios could be broken with an analysis of the radius valley in three dimensions. Hence, we implement an SVM in three dimensions: planet radius  $R_p$ , orbital period  $P$ , and mass of the host star  $M_*$ , to fit the radius valley in the form of a plane. We perform bootstrapping with 1000 sample sets as per previous. We obtain the relation

$$\log_{10} (R_p / R_{\oplus}) = A \log_{10} (P / \text{days}) + B \log_{10} (M_* / M_{\odot}) + C \quad (11)$$

with  $A = -0.09^{+0.02}_{-0.03}$ ,  $B = 0.21^{+0.06}_{-0.07}$ , and  $C = 0.35^{+0.02}_{-0.02}$ . An illustration of the SVM plane is shown in Fig. 6.

We also investigate the radius valley location in the  $R_p$ – $S$ – $M_*$  space. Fig. 6 (right-hand panel) shows the radius valley location in this space. We find

$$\log_{10} (R_p / R_{\oplus}) = A \log_{10} (S / S_{\oplus}) + B \log_{10} (M_* / M_{\odot}) + C \quad (12)$$

with  $A = 0.07 \pm 0.02$ ,  $B = -0.01^{+0.07}_{-0.09}$ , and  $C = 0.11^{+0.04}_{-0.05}$ .

### 3.5 Radius valley dependence on stellar age

We investigate the location of the radius valley as a function of stellar age. We obtain the stellar ages from F18. Kepler-174 does not have stellar age data from this source; hence, we omit Kepler-174 b and Kepler-174 c in our analysis with stellar age.

Fitting the valley with the SVM, we obtain

$$\log_{10} (R_p / R_{\oplus}) = m \log_{10} (\text{Age} / \text{Gyr}) + c \quad (13)$$

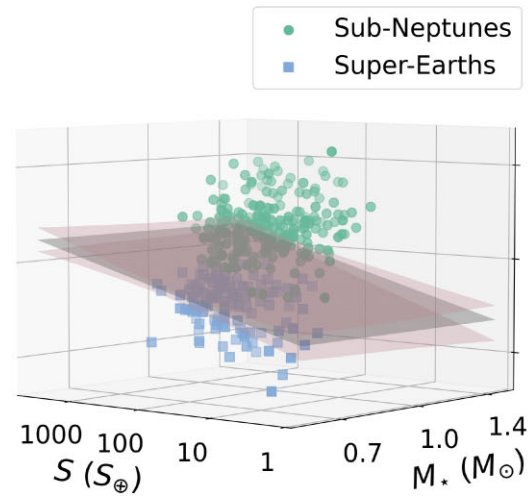


**Figure 6.** Plot of planet radius against orbital period and mass of host star (left-hand panel), and planet radius against incident flux and stellar mass (right-hand panel). The grey plane shows the radius valley location determined with the SVM in three dimensions, with the  $\pm 1\sigma$  uncertainties shown in pink. The uncertainties on individual planet parameters are not displayed in the interest of clarity.

with  $m = 0.02_{-0.02}^{+0.01}$  and  $c = 0.26_{-0.01}^{+0.01}$ , showing no significant correlation with the radius valley location in two-dimensional space. The result is displayed in Fig. 7 (left-hand panel).

We further investigate whether the radius valley *depth* may be a function of stellar age. To do so, we generate histograms, similar to Fig. 4, split into different stellar age subsamples. Fig. 8 (left-hand panel) shows that for older stars, the radius valley location shifts to higher  $R_p$ , and the radius valley becomes shallower. The change in the  $E$  metric is reported in Table 4. These findings suggest that the radius valley has a dependence on the age of the host stars.

We further plot the radius valley in  $R_p$ – $P$ –age space, and fit the valley with the SVM, as shown in Fig. 9 (left-hand panel). We find

$$\log_{10}(R_p/R_\oplus) = A \log_{10}(P/\text{days}) + B \log_{10}(\text{Age/Gyr}) + C \quad (14)$$

with  $A = -0.10 \pm 0.02$ ,  $B = 0.03_{-0.03}^{+0.02}$ , and  $C = 0.34_{-0.02}^{+0.03}$ .

We can also combine  $R_p$ ,  $P$ ,  $M_*$ , and stellar age, and determine the radius valley with a four-dimensional SVM, as shown in Fig. 10. The resulting equation representing the radius valley is in the form of a four-dimensional hyperplane

$$\log_{10}(R_p/R_\oplus) = A \log_{10}(P/\text{days}) + B \log_{10}(M_*/M_\odot) + C \log_{10}(\text{Age/Gyr}) + D \quad (15)$$

with  $A = -0.096_{-0.027}^{+0.023}$ ,  $B = 0.231_{-0.064}^{+0.053}$ ,  $C = 0.033_{-0.025}^{+0.017}$ , and  $D = 0.339_{-0.018}^{+0.026}$ . These results imply there is strong evidence the radius valley location is dependent on  $P$  and  $M_*$ , and weak evidence for its dependence on stellar age ( $>1\sigma$ ). These values are also consistent within  $1\sigma$  with their corresponding dependencies in two and three dimensions (see Table 3).

### 3.6 Radius valley dependence on stellar metallicity

We perform a similar analysis in terms of the stellar metallicity. As for age, we obtain the stellar metallicity from V18 if available, and F18 otherwise. We find

$$\log_{10}(R_p/R_\oplus) = m[\text{Fe}/\text{H}] + c \quad (16)$$

with  $m = 0.06_{-0.08}^{+0.06}$  and  $c = 0.26_{-0.01}^{+0.01}$ , again displaying no significant correlation with the radius valley location in two-dimensional space.

We divide the planet population into two groups, based on the median  $[\text{Fe}/\text{H}] = 0.06$ . The adjusted histograms in Fig. 8 (right-hand panel) show that the super-Earth peak is lower for metal-poor stars. The  $E$  values are reported in Table 5.

We perform a similar SVM analysis in  $R_p$ – $P$ – $[\text{Fe}/\text{H}]$  space (shown in right-hand panel of Fig. 9), and find

$$\log_{10}(R_p/R_\oplus) = A \log_{10}(P/\text{days}) + B[\text{Fe}/\text{H}] + C \quad (17)$$

with  $A = -0.10 \pm 0.03$ ,  $B = 0.03_{-0.04}^{+0.03}$ , and  $C = 0.36_{-0.03}^{+0.02}$ . These values imply that we find no evidence that the radius valley location depends on stellar metallicity.

## 4 DISCUSSION

### 4.1 $R_p$ – $P$ relation suggests a thermally driven mass-loss model

As presented in Section 3.2, we observe the radius valley scales as  $m = d\log R_p/d\log P = -0.11 \pm 0.02$ . This negative period-dependence is a robust finding which remains roughly similar even when other parameters are included in the fit (see Table 3).

Different theoretical mechanisms to create the radius valley result in a different slope as a function of orbital period. For example, Lopez & Rice (2018) predicted that if the rocky planets are core remnants of sub-Neptunes with evaporated atmospheres, the radius valley location should decrease with increasing orbital period, with  $m = -0.09$ , whereas if those rocky planets were formed after disc dissipation (i.e. late gas-poor formation), the radius valley location tends to larger planetary radii at longer orbital periods, with  $m = 0.11$ . Similarly, Owen & Wu (2017) predicted a negative period–radius valley slope for a photoevaporation model, with  $-0.25 \leq m \leq -0.16$  depending on the photoevaporation efficiency. If the radius valley is thermally driven but powered by the core rather than photoevaporation, the slope would be similarly negative, with e.g. Gupta & Schlichting (2019) predicting that  $m \approx -0.11$  in this case. Theoretically predicted slopes for different formation mechanisms are summarized in Table 6.

Our observed negative slope is consistent with thermally driven mass-loss models but inconsistent with late gas-poor formation models. We can also compare our observed slope with other observational studies (see again Table 6). The period-radius slope was first observed by V18, who used the SVM approach that we adopted here and who found  $m = -0.09_{-0.04}^{+0.02}$ . A different approach was followed by Martinez et al. (2019), who divided their planetary sample into 10 bins with equal number of planets, determined the minimum radius in each bin, and fitted a linear relationship to obtain equation (4). These two approaches led to a consistent result, with  $m = -0.11 \pm 0.02$ . MacDonald (2019) adopted machine-learning approaches, and report  $m = -0.319_{-0.116}^{+0.088}$ . The above studies all focus on samples of FGK stars, where various approaches to model the valley’s location appear to result in negative slopes with consistent magnitude, matching thermally driven atmospheric loss models.

For smaller and cooler (M-type) stars, Cloutier & Menou (2020) found a positive slope ( $m = 0.058 \pm 0.022$ ) using a method similar to Martinez et al. (2019), suggesting for these stars the valley may be the result of gas-poor formation rather than being thermally driven. Van Eylen et al. (2021) used the SVM approach to measure the M-dwarf valley and found a negative slope instead, of  $-0.11_{-0.04}^{+0.05}$ . Luque & Pallé (2022) used the `gapfit` package (Lloyd et al. 2020) and found  $m = -0.02 \pm 0.05$ . A recent study by Petigura et al. (2022) also included M-type stars in addition to FGK stars, and they found  $m = -0.11 \pm 0.02$  for this sample. Our sample does not include M-type stars but does span a mass range from about 0.6 to  $1.4M_*$ .

To investigate whether the slope of  $m$  changes with stellar mass within our sample, we split our planetary sample into two groups:  $M_* \geq 1M_\odot$ , and  $M_* < 1M_\odot$ . We determine the  $R_p$ – $P$  relation separately for these two groups with the same methods as above. We find for  $M_* \geq 1M_\odot$ ,  $m = -0.07_{-0.04}^{+0.02}$ , and  $c = 0.35_{-0.02}^{+0.03}$ ; for  $M_* < 1M_\odot$ ,  $m = -0.11_{-0.07}^{+0.02}$ , and  $c = 0.35_{-0.02}^{+0.05}$ . These results are shown in Fig. 11. The two values are in agreement within  $1\sigma$ , suggesting that within our sample, the radius valley location as a function of orbital period is inconsistent with the gas-poor formation scenario.

We can also look at the slope of the valley as a function of incident flux ( $S$ ) rather than orbital period. By Kepler’s third law (as shown in equation 7), planets at longer orbital periods are located further away from the planet, thus the incident flux  $S$  is lower for planets with larger star–planet distances, as shown in equation (5). Hence, we expect for a thermally driven planetary mass-loss scenario, the radius valley location tends to larger planetary radii for higher  $S$ .

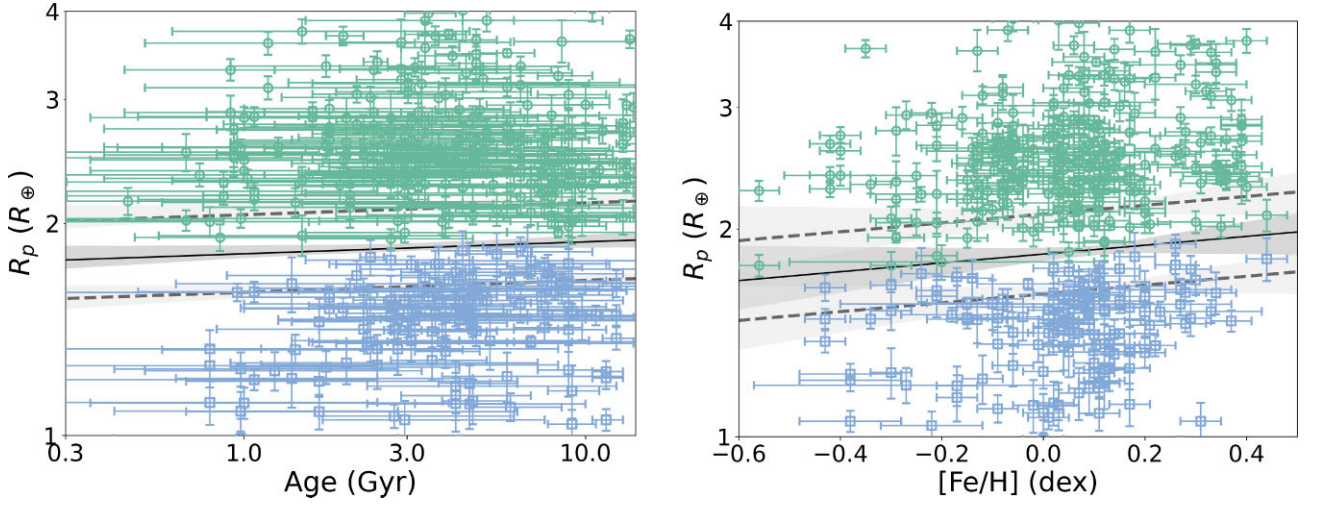


**Figure 7.** Same as Fig. 5, but for stellar age (left-hand panel,  $m = 0.01^{+0.01}_{-0.02}$ ,  $c = 0.26^{+0.01}_{-0.01}$ ), and stellar metallicity [Fe/H] (right-hand panel,  $m = 0.06^{+0.06}_{-0.08}$  and  $c = 0.26^{+0.01}_{-0.01}$ ).

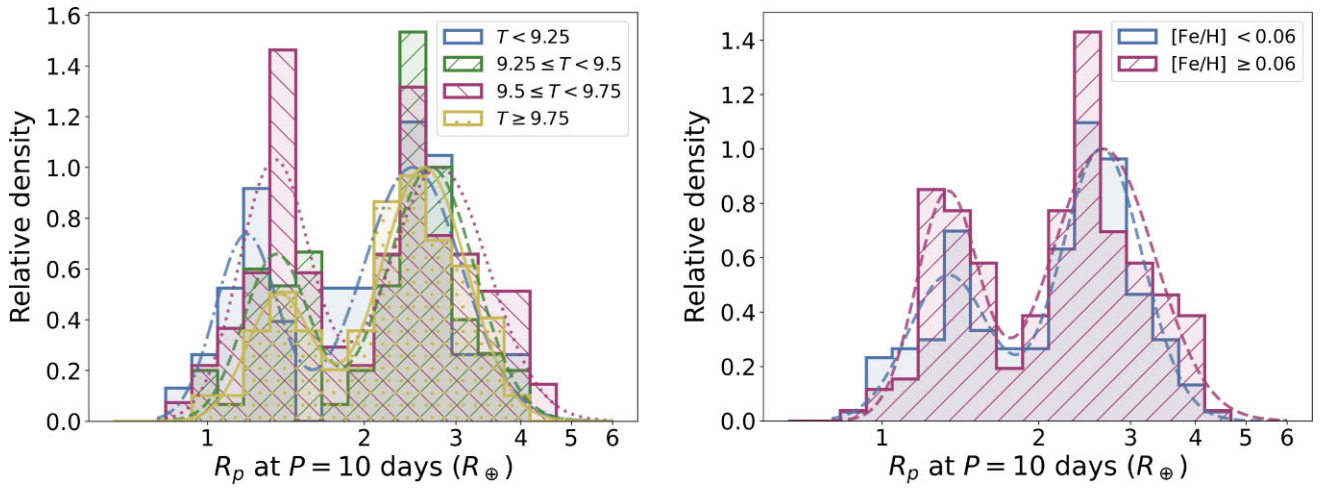


**Figure 8.** Same as Fig. 4, but separated into different stellar ages (left-hand panel), and metallicities (right-hand panel). Here,  $T = \log_{10}(\text{Age}/\text{yr})$ . The histograms are normalized such that the relative density of the sub-Neptune peak equals to unity.

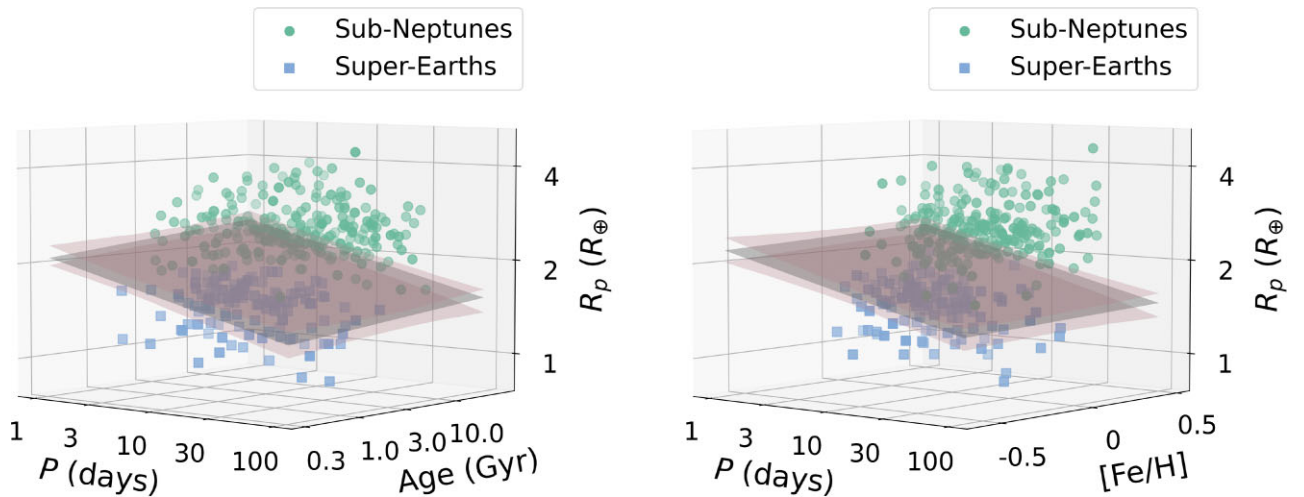


**Figure 9.** Same as Fig. 6, but in  $R_p$ - $P$ -age space (left-hand panel) and  $R_p$ - $P$ -[Fe/H] space (right-hand panel).



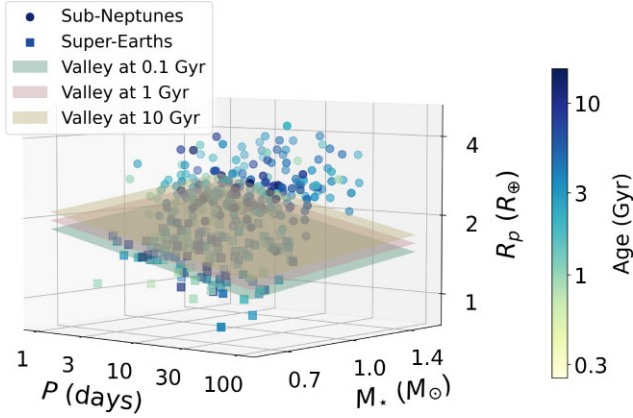


**Figure 10.** Radius valley location in terms of orbital period, stellar mass, and stellar age. The colour bar represents the age of the planetary host stars, and planes of different colours indicate the radius valley location for different stellar ages.

We observe this positive relationship in this work, in agreement with other previous observations as shown in Table 7, and consistent with thermally driven mass-loss models which is also shown in radius-period space.

#### 4.2 $R_p$ – $M_\star$ relation supports a thermally driven mass-loss model

As presented in Section 3.4, we find that in two dimensions,  $m = d \log R_p / d \log M_\star = 0.23^{+0.09}_{-0.08}$ .

A stellar mass dependence has been predicted by radius valley models. Both thermally driven mass-loss models predict a similar dependence of the valley on stellar mass. For example, Rogers et al. (2021) predicted  $m = 0.29$  and  $0.32$  for photoevaporation (Owen & Wu 2017) and core-powered mass-loss models (Gupta & Schlichting 2019, 2020), respectively. Our results are consistent with both sets of models within  $1\sigma$ .

A stellar mass dependence was observed by Berger et al. (2020), who find  $m = 0.26^{+0.21}_{-0.16}$  by fitting the minima of the two-dimensional KDE in  $R_p$ – $M_\star$  space. A recent study by Petigura et al. (2022), similarly following a binning approach and incorporating data from Data Release 2 (DR2) of the *California–Kepler Survey* for cooler stars, estimated  $m = 0.18^{+0.08}_{-0.07}$ . It is therefore reassuring to see that despite the different methods adopted here, the slope derived in this work is consistent with both of these studies within  $1\sigma$ . For lower mass stars, Luque & Pallé (2022) found  $m = 0.08 \pm 0.12$ ; this may be inconsistent with our results at  $1\sigma$ , however, the stellar mass range they studied is significantly lower than that in our sample with no overlaps. The results are summarized in Table 8.

When extending our analysis to three dimensions as a function of  $P$  and  $M_\star$ , we obtain  $A = (\partial \log R_p / \partial \log P)_{M_\star} = -0.09^{+0.06}_{-0.03}$ ,  $B = (\partial \log R_p / \partial \log M_\star)_P = 0.21^{+0.06}_{-0.08}$  from determining the radius valley location in the  $R_p$ – $P$ – $M_\star$  space. Note that this is different to the total derivative  $d \log R_p / d \log M_\star$  in two dimensions (shown in Table 3). Based on the models of photoevaporation (Owen & Wu 2017; Owen & Adams 2019; Mordasini 2020) and core-powered mass-loss (Gupta & Schlichting 2019, 2020), Van Eylen et al. (2021) predicted  $B = 0.19$  for a photoevaporation model, and  $B = 0.33$  for a core-powered mass-loss model. Our resulting posterior distribution of  $A$  and  $B$  determined from the bootstrapping presented in Section 3.4, as shown in Fig. 12, is consistent with both the

photoevaporation and core-powered mass-loss cases at  $2\sigma$ , hence we are unable to distinguish between the two models in this particular parameter space.

Rogers et al. (2021) proposed an analysis of the radius valley in  $R_p$ – $S$ – $M_\star$  space that could distinguish between the two different thermally driven mass-loss mechanisms. Using theoretical models, they predicted the radius valley scales as a function of  $S$  and  $M_\star$  as equation (11), with  $A = (\partial \log R_p / \partial \log S)_{M_\star} \simeq 0.12$  and  $B = (\partial \log R_p / \partial \log M_\star)_S \simeq -0.17$  for a photoevaporation model, and  $A \simeq 0.08$  and  $B \simeq 0.00$  for a core-powered mass-loss model. Again, we plot the posterior distributions of  $A$  and  $B$ , as shown in Fig. 13, and observe that our results are consistent with the core-powered mass-loss case well within  $1\sigma$ . For the photoevaporation scenario, our values overlap with the theoretical predictions at the edge of the  $2\sigma$  confidence interval. Rogers et al. (2021) also measured the planet density of the CKS (F18), and the *Gaia–Kepler Survey* (GKS, Berger et al. 2020), in  $R_p$ – $S$ – $M_\star$  space. They found for the CKS data,  $A = 0.13^{+0.03}_{-0.05}$ ,  $B = -0.21^{+0.33}_{-0.39}$ , and for the GKS data,  $A = 0.10^{+0.03}_{-0.02}$ ,  $B = -0.03^{+0.10}_{-0.12}$ . Our results are in agreement with both the CKS and GKS values, and our measurements have smaller uncertainties.

There are some caveats to this comparison between our observation results and theoretical models. First, the thermally driven mass-loss models predict the slope of the bottom of the valley (V18; Rogers et al. 2021), whereas our SVM finds the slope for the middle of the radius valley. Some studies have suggested a different planet size dependence with orbital period for super-Earths and sub-Neptunes (e.g. Petigura et al. 2022), hence these two slopes may not be equal. Since the radius valley is not completely empty, the bottom of the radius valley is not clearly defined, and there would be challenges locating and fitting the bottom of the radius valley. As a result, our observed values may not be fully comparable with theoretical model values. Furthermore, the method of extracting the radius valley is prone to transit biases, which we do not correct for in this work. Rogers et al. (2021) showed that even when modelling synthetic transit surveys based on evolving planets with theoretical models, the resulting posteriors may not be fully consistent with the theoretically predicted slope. Further work, such as generating synthetic surveys from both photoevaporation and core-powered mass-loss models based on conditions similar to that of our sample in a method similar to that performed in Rogers et al. (2021), and fitting the valley with the same method as in this work, or analysing more planets around stars in a larger mass range, is required to compare our observations to theoretical models in a homogeneous way.

#### 4.3 Deeper radius valley suggests a homogeneous initial planetary core composition

We now turn to the depth of the radius valley. Using the previously defined depth metric ( $E$ , equations 9 and 10), we find a valley depth of  $E_{\text{avg}} = 2.98^{+0.60}_{-0.47}$  (see Section 3.3). We can compare this depth to the valley observed by F18. Shifting the planets along the slope calculated in Section 3.2, and applying the same metric to their filtered sample of 907 planets, we calculate  $E_{\text{SN}} = 1.99^{+0.26}_{-0.23}$ ,  $E_{\text{SE}} = 2.28^{+0.31}_{-0.27}$ , giving  $E_{\text{avg}} = 2.14^{+0.26}_{-0.21}$  for that sample. For V18, we shift the planets according to the slope obtained in their study, i.e.  $m = -0.09^{+0.02}_{-0.04}$ , and we find  $E_{\text{SN}} = 7.11^{+4.70}_{-2.49}$ ,  $E_{\text{SE}} = 4.75^{+3.42}_{-1.70}$ , giving  $E_{\text{avg}} = 6.05^{+3.87}_{-2.14}$ . These values imply that compared to F18, we observe a deeper radius valley. On the other hand, the radius valley appears less deep than observed by V18 for a smaller sample. This finding is visualized in Fig. 14, which shows the adjusted histograms of the sample studied here next to the F18 and the V18 samples.

**Table 3.** Dependencies of the radius valley in  $n$  dimensions ( $m_i$ ), given by the equation  $\log_{10}(R_p/R_\oplus) = \sum_{i=1}^n m_i x_i$ , with different parameter combinations  $x_i$ . The methods used to obtain the equation of the radius valley hyperplanes are also given, where SVM and KDE stand for the SVM and fitting the minima of the kernel density estimates, respectively.

Dimensions	$\log_{10}(P/d)$	$\log_{10}(S/S_\oplus)$	$\log_{10}(M/M_\odot)$	$\log_{10}(\text{Age/Gyr})$	[Fe/H]	Intercept	Method
2	$-0.11^{+0.02}_{-0.02}$	$0.07^{+0.02}_{-0.01}$	$0.23^{+0.09}_{-0.08}$	$0.02^{+0.01}_{-0.02}$	$0.06^{+0.06}_{-0.08}$	$0.37^{+0.02}_{-0.03}$	SVM
	$-0.12^{+0.03}_{-0.05}$					$0.37^{+0.05}_{-0.03}$	KDE
						$0.11^{+0.03}_{-0.04}$	SVM
						$0.27^{+0.01}_{-0.01}$	SVM
						$0.26^{+0.01}_{-0.01}$	SVM
						$0.26^{+0.01}_{-0.01}$	SVM
3	$-0.09^{+0.02}_{-0.03}$	$0.07^{+0.02}_{-0.02}$	$-0.01^{+0.07}_{-0.09}$	$0.03^{+0.02}_{-0.03}$	$0.03^{+0.03}_{-0.04}$	$0.35^{+0.02}_{-0.03}$	SVM
						$0.11^{+0.04}_{-0.05}$	SVM
	$-0.10^{+0.02}_{-0.02}$					$0.34^{+0.03}_{-0.02}$	SVM
4	$-0.10^{+0.03}_{-0.03}$	$0.231^{+0.053}_{-0.064}$	$0.033^{+0.017}_{-0.025}$			$0.36^{+0.02}_{-0.03}$	SVM
	$-0.096^{+0.023}_{-0.027}$					$0.339^{+0.026}_{-0.018}$	SVM

**Table 4.**  $E$  values of the radius valley for different ages of the host stars.  $E_{\text{avg}} = (E_{\text{SN}} + E_{\text{SE}})/2$ .

$\log_{10}(\text{age/yr})$	Age (Gyr)	$N_{\text{planets}}$	$E_{\text{SN}}$	$E_{\text{SE}}$	$E_{\text{avg}}$
<9.25	<1.78	53	4.93	3.64	4.28
9.25–9.5	1.78–3.16	95	4.69	3.08	3.89
9.5–9.75	3.16–5.62	114	3.22	3.32	3.27
>9.75	>5.62	111	2.21	4.40	3.30

**Table 5.**  $E$  values of the radius valley for different stellar metallicities.  $E_{\text{avg}} = (E_{\text{SN}} + E_{\text{SE}})/2$ .

[Fe/H]	$N_{\text{planets}}$	$E_{\text{SN}}$	$E_{\text{SE}}$	$E_{\text{avg}}$
<0.06	181	4.10	2.20	3.15
$\geq 0.06$	194	3.28	2.78	3.03

To investigate the reason for observing a deeper valley than F18, we compare the 211 planets common in both our sample and the filtered sample of F18. To investigate the role of transit fitting, we convert all our  $R_p/R_\star$  into  $R_p$  using  $R_\star$  from F18 (even when V18 values are available). The results are shown in Fig. 15, which compares the same planets with the same stellar parameters but different transit fitting. We observe that in this case, the  $R_p$  of 56 (27 per cent) and 24 (11 per cent) planets change by  $>2\sigma$  and  $>3\sigma$ , respectively, compared to the values reported in F18. We find for this common planetary sample, for our planetary parameters,  $E_{\text{SN}} = 3.63^{+1.02}_{-0.70}$ ,  $E_{\text{SE}} = 2.95^{+0.86}_{-0.63}$ , giving  $E_{\text{avg}} = 3.29^{+0.91}_{-0.59}$ , whereas for parameters from F18,  $E_{\text{SN}} = 2.40^{+0.59}_{-0.47}$ ,  $E_{\text{SE}} = 1.93^{+0.49}_{-0.39}$ , giving  $E_{\text{avg}} = 2.18^{+0.49}_{-0.42}$ . These findings suggest that our updated transit fittings are directly responsible for deepening (although not fully emptying) the radius valley.

A deeper radius valley is associated with a more homogeneous planet core composition. For example, in photoevaporation models, the radius valley position is dependent on the mass of the planet core ( $M_c$ ), and the density of a  $1M_\oplus$  core of a particular core composition ( $\rho_{M_\oplus}$ ), as

$$R_{\text{valley}} \propto \rho_{M_\oplus}^{-1/3} M_c^{1/4}. \quad (18)$$

Hence, if  $R_{\text{valley}}$  is known, and the planets' mean masses are known, the planetary core compositions could be deduced (Owen & Wu 2017).

Using the above relation, if the planetary cores were icy at formation, the radius valley would be located at a higher planetary radius than if the cores were rocky/terrestrial at formation. Hence, if the planetary cores are of mixed composition, a superposition of the two models would be predicted, and we would expect the radius valley to be smeared and less distinct, as each type of planet would have its own 'radius valley' at a different location (Owen & Wu 2017). Our deep radius valley found in this work implies the opposite case, where the planetary cores are more similar in composition. In this scenario, planets inside the valley may have a different (e.g. icy) composition.

Owen & Wu (2017) compared their models to observations, and found that the planet compositions are more likely to be Earth-like (i.e. rocky), but that the apparent shallowness of the valley suggested a wide distribution of iron fractions ( $f_{\text{Fe}}$ ) in their cores, as planets with a single value iron fraction ( $f_{\text{Fe}} = 0.5$ ) produces a deeper valley compared to planets with a uniform distribution ( $f_{\text{Fe}} \in [0, 1]$ ). Comparing our finding of a deeper valley to models in Owen & Wu (2017) would indicate that the planet compositions are more likely to have similar iron fractions with a narrower spread.

Similarly, in the core-powered mass-loss model, the location of the radius valley scales as

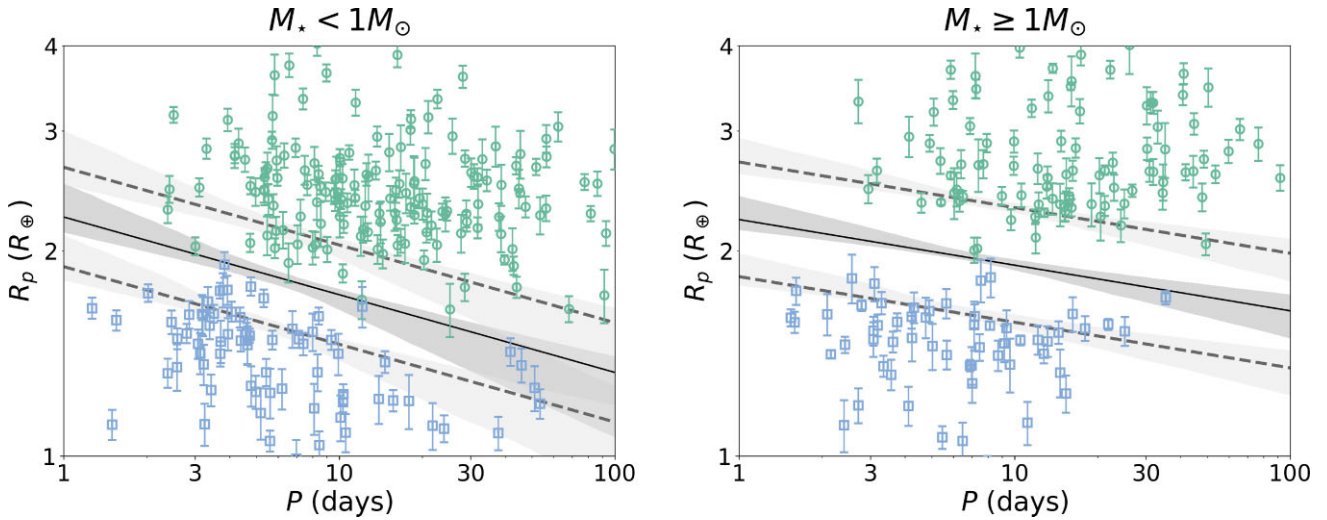
$$R_{\text{valley}} \propto \rho_c^{-4/9} \quad (19)$$

where  $\rho_c$  is the planet core density (Gupta & Schlichting 2019). The same reasoning as the photoevaporation case then applies: given the larger  $\rho_c$  for icy cores, planets with homogeneous icy cores will produce a radius valley at larger planetary radii compared to rocky/terrestrial cores, implying that the radius valley would be smeared if planetary cores are of inhomogeneous compositions. Our deep radius valley supports the opposite case, i.e. a similar planetary core composition.

Fig. 16 shows the stellar parameter distributions for the planet host stars in the three planet samples, and the mean and median values are listed in Table 9. We notice a similar stellar parameter range between this work and F18; however, the stars in V18 are brighter, have a larger mean radius and mass, and higher effective temperature. This is likely due to V18 selecting stars which display strong asteroseismic

**Table 6.** Slope of the radius valley on the radius–period plane from various sources.

Source		$m = d \log R_p / d \log P$	Stellar type
Observations	This work	$-0.11^{+0.02}_{-0.02}$	FGK
	V18	$-0.09^{+0.02}_{-0.04}$	FGK
	Martinez et al. (2019)	$-0.11^{+0.02}_{-0.02}$	FGK
	MacDonald (2019)	$-0.319^{+0.088}_{-0.116}$	FGK
	Cloutier & Menou (2020)	$0.058^{+0.022}_{-0.022}$	M
	Van Eylen et al. (2021)	$-0.11^{+0.05}_{-0.04}$	M
	Petigura et al. (2022)	$-0.11^{+0.02}_{-0.02}$	FGKM
	Luque & Pallé (2022)	$-0.02^{+0.05}_{-0.05}$	M
Source		$m = d \log R_p / d \log P$	Model
Theory	Owen & Wu (2017)	$-0.25 \leq m \leq -0.16$	Photoevaporation
	Lopez & Rice (2018)	-0.09	Photoevaporation
		0.11	Gas-poor formation
	Gupta & Schlichting (2019)	-0.11	Core-powered mass-loss
	Rogers et al. (2021)	-0.16	Photoevaporation
		-0.11	Core-powered mass-loss

**Figure 11.** Radius valley position for planets with host star mass  $M_* < 1 M_\odot$  (left-hand panel), and  $M_* \geq 1 M_\odot$  (right-hand panel). For  $M_* < 1 M_\odot$ ,  $m = -0.11^{+0.02}_{-0.07}$ , and  $c = 0.35^{+0.05}_{-0.02}$ ; for  $M_* \geq 1 M_\odot$ ,  $m = -0.07^{+0.02}_{-0.04}$ , and  $c = 0.35^{+0.03}_{-0.02}$ . The green and blue points show planets above and below the radius valley, respectively. The grey-shaded region represents the  $\pm 1\sigma$  uncertainty in the radius valley position determined with bootstrapping.**Table 7.** Same as Table 6, but for the radius valley slope on the radius–incident-flux plane.

Source		$m = d \log R_p / d \log S$	Stellar type
Observations	This work	$0.07^{+0.02}_{-0.01}$	FGK
	Martinez et al. (2019)	$0.12 \pm 0.02$	FGK
	Cloutier & Menou (2020)	$-0.060 \pm 0.025$	M
	Petigura et al. (2022)	$0.06 \pm 0.01$	FGKM
	Luque & Pallé (2022)	$0.02 \pm 0.02$	M

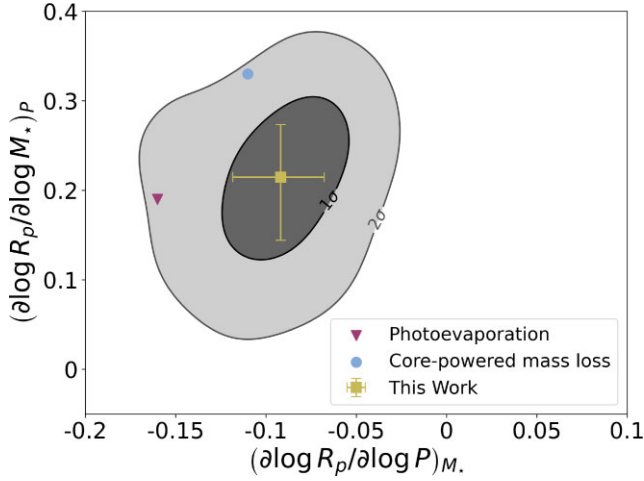
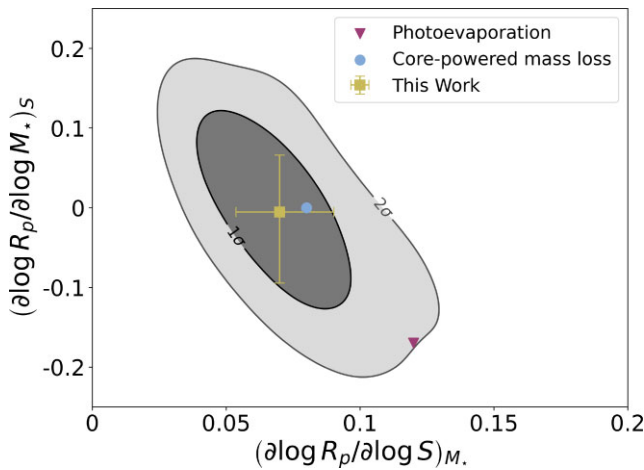
signals, which usually are brighter and larger stars. This observation may indicate that the radius valley of such stars are emptier; however, the details are left for future studies.

Despite our new results revealing that the radius valley deepens by refitting planets with 1-min short cadence light curves, it is still uncertain whether the difference between results from this work and F18 is solely due to the cadence in transit data used, as different

methods are used in the transit fitting process. Mullally et al. (2015) fitted planets using the method described in Rowe et al. (2014), which first fits a multiplanet transit model to the light curves, with fixed limb-darkening parameters from Claret & Bloemen (2011), and subsequently fitting for each planet in a system independently by removing photometric contributions of other planets based on the parameters from the multiplanet fit. In our work, we fit planets in

**Table 8.** Same as Table 6, but for the radius valley slope on the radius–stellar–mass plane.

	Source	$m = d \log R_p / d \log M_*$	Stellar type
Observations	This work	$0.23^{+0.09}_{-0.08}$	FGK
	Berger et al. (2020)	$0.26^{+0.21}_{-0.16}$	FGKM
	Petigura et al. (2022)	$0.18^{+0.08}_{-0.07}$	FGKM
	Luque & Pallé (2022)	$0.08^{+0.12}_{-0.12}$	M
	Source	$m = d \log R_p / d \log M_*$	Model
Theory	Gupta & Schlichting (2020)	0.33	Core-powered mass-loss
	Rogers et al. (2021)	0.29	Photoevaporation
		0.32	Core-powered mass-loss

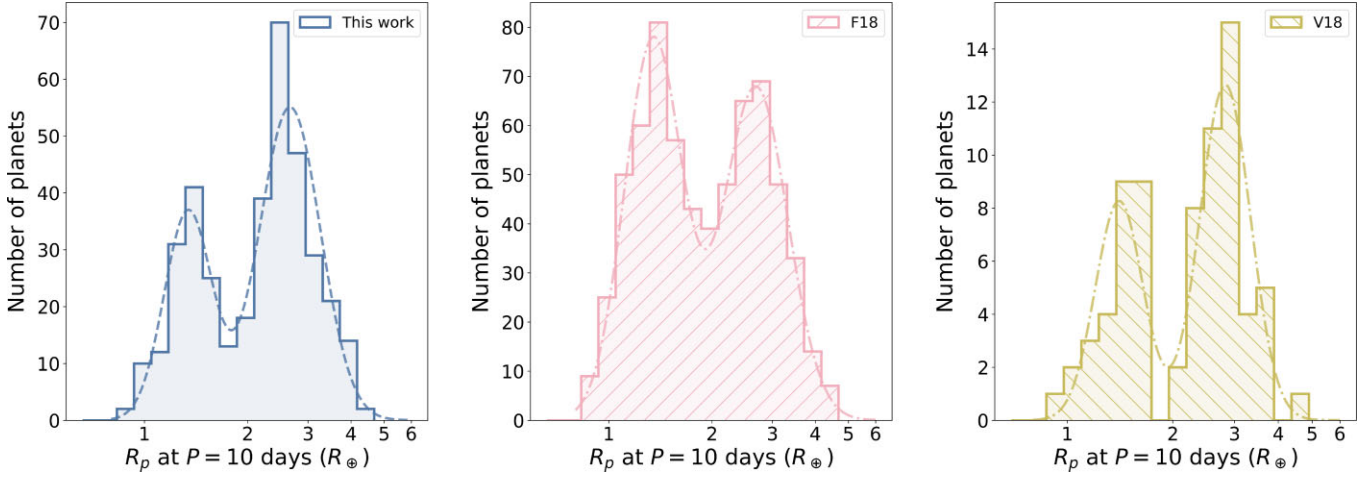

**Figure 12.** Posterior distributions of the radius valley location dependence with respect to orbital period at constant stellar mass  $(\partial \log R_p / \partial \log P)_{M_*}$ , and stellar mass at constant orbital period  $(\partial \log R_p / \partial \log M_*)_P$ . The dark- and light-coloured shades represent the  $1\sigma$  and  $2\sigma$  uncertainties, respectively. The theoretical models of photoevaporation and core-powered mass-loss are taken from Van Eylen et al. (2021).

**Figure 13.** Same as Fig. 12, but for  $(\partial \log R_p / \partial \log S)_{M_*}$  and  $(\partial \log R_p / \partial \log M_*)_S$ .

multiplanet systems simultaneously, such that each system shares the same stellar parameters, including limb-darkening parameters and stellar density. Mullally et al. (2015) assumed a circular orbit when performing the transit fits. On the contrary, we leave orbital eccentricity  $e$  as a free parameter, and place a prior on  $e$  based on the expected distribution from Van Eylen et al. (2019) and the stellar density  $\rho_*$  from F18. However, most of the planets in our sample have near-circular orbits, with over 85 per cent of planets having  $e < 0.1$ . Therefore planetary orbital eccentricity is not sufficient to explain the difference between the two results. The possible presence of TTVs also does not contribute to the discrepancy as planets with known TTVs are excluded in our like-for-like planet comparisons. In fact, when fitting transits using identical methods, precisions in  $R_p/R_*$  obtained from fitting transit light curves of shorter cadences have been found to substantially improve, compared to 30-min cadence light curves (Camero, Ho & Van Eylen, in preparation). We therefore expect the photometry cadence to contribute significantly to the difference in the views of the radius valley. Further work, such as refitting the long cadence data of the same planet population with identical transit fitting methods, is needed to further investigate the effect of light curve cadence on planet parameter estimates and the radius valley. We leave such considerations for future studies.

#### 4.4 Radius valley relation with stellar age consistent with core-powered mass-loss model

In Section 3.5, we present a positive relationship between the radius valley location and stellar age. Photoevaporation is predicted to occur in the first 100 Myr of the planet’s formation (Owen & Wu 2017), well before observations are able to detect the evolution signals, whereas core-powered mass-loss occurs throughout the main-sequence lifetime of the stars, on Gyr time-scales (Ginzburg, Schlichting & Sari 2016; Gupta & Schlichting 2019, 2020). Hence, in the photoevaporation case, the radius valley is expected to be located at a constant radius. On the other hand, in the core-powered mass-loss case, the radius valley shifts to higher planet radii for older systems, as the atmospheres of planets with more massive cores are stripped off later in the evolution process than their less-massive counterparts (e.g. David et al. 2021; Rogers & Owen 2021).

Our results reveal a weak positive radius valley dependence on the stellar age, which is consistent with the core-powered mass-loss scenario, as is the observed radius valley dependence on stellar mass as discussed in Section 4.2. However, a small age dependence does not preclude photoevaporation, since even in this scenario a subset of planets may still lose their atmospheres and evolve at Gyr time-scales (David et al. 2021; Rogers et al. 2021), and we are unable to observe stars younger than 100 Myr and hence cannot rule out the



**Figure 14.** Histogram of planet radii, adjusted to  $P = 10$  d for the planetary population in this work (left-hand panel, identical to Fig. 4), F18 (centre panel), and V18 (right-hand panel). Planets in this work and F18 are shifted according to the slope defined in Section 3.2 with the SVM (i.e.  $-0.11^{+0.02}_{-0.02}$ ), whereas planets in V18 are shifted according to the slope found in V18 (i.e.  $m = -0.09^{+0.02}_{-0.04}$ ). The  $E$  metrics defining the average peak-to-valley ratio are  $2.98^{+0.60}_{-0.47}$ ,  $2.14^{+0.26}_{-0.21}$ , and  $6.05^{+3.87}_{-2.14}$ , respectively.

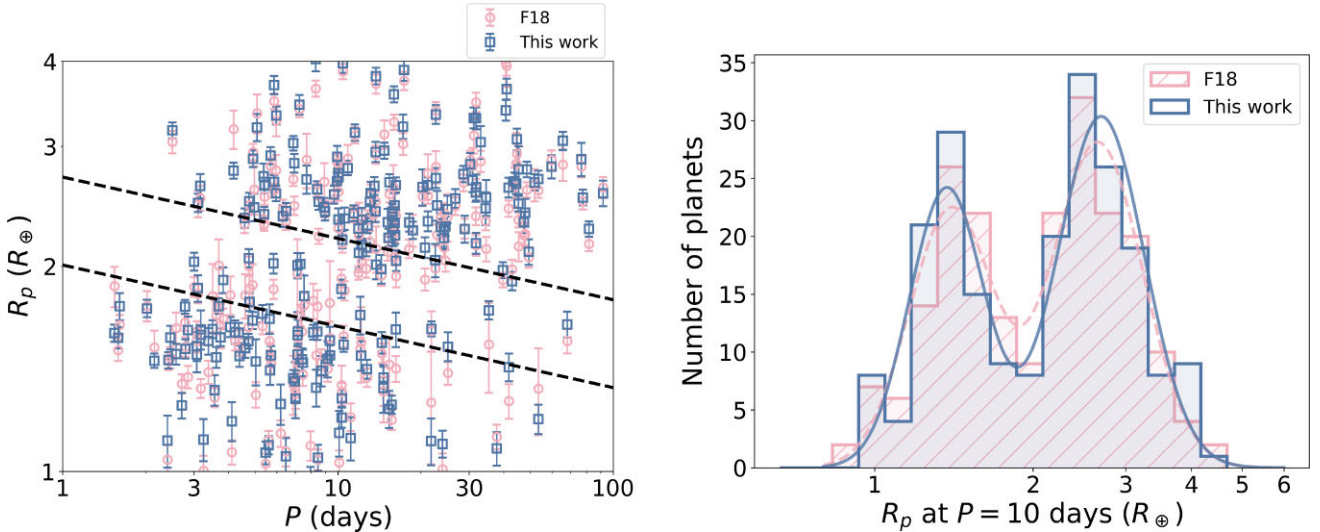


**Figure 15.** Left-hand panel: radius-period plot of the 211 planets common to this work (blue) and F18 (red), using the same stellar radii to calculate planetary radii. Right-hand panel: same as Fig. 14, but the planetary population is filtered to the 211 common planets in both samples. Planets in both samples are adjusted to equivalent radii at  $P = 10$  d according to the slope calculated in Section 3.2 with the SVM. The red and blue histograms are produced with the parameters obtained from F18 and this work, respectively. The histograms and fitting with the Gaussian mixture model show that the observed valley is deeper in this work.

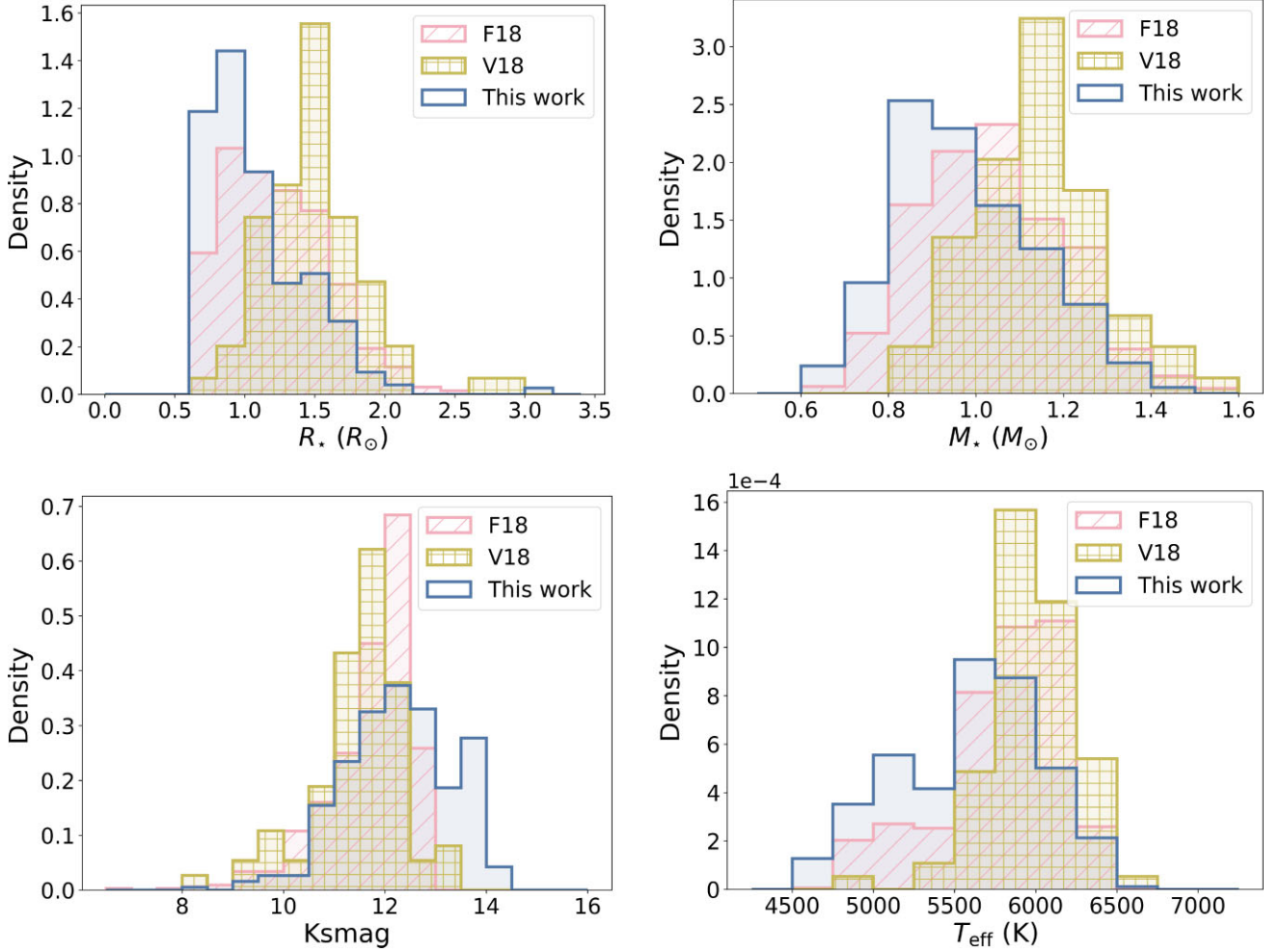
possibility of a dominant photoevaporation effect on planets at the early stages of the stars’ lifetime. Also, stellar age measurements are highly uncertain; the mean percentage uncertainty in stellar age for our sample is 54 per cent, hence there is also a probability that some stars are younger than observed.

Table 10 lists the 50 planets located inside the radius valley in our sample. To do so, we here defined the new radius valley region as the area bounded by the two lines passing through the supporting vectors in the 4D SVM model in Section 3.5, given by equation (15) with  $A = -0.096$ ,  $B = 0.231$ ,  $C = 0.033$ ,  $D_{\text{lower}} = 0.272$  for the lower line, and  $D_{\text{upper}} = 0.405$  for the upper line. These planets are potentially interesting for future characterization study as their atmospheres and interiors may provide additional insights regarding formation and evolution mechanisms.

#### 4.5 Radius valley depth varies with stellar metallicity

In Section 3.6, we show a higher average  $E$  value (i.e. a deeper radius valley) for planets around metal-poor stars. This seems to contradict the suggestion that the radius valley is deeper for planets around metal-rich stars (Owen & Murray-Clay 2018). However, we note from Fig. 17, that in our sample, the metal-rich host stars span a wider range of stellar masses, due to lack of metal-poor stars with large radii. As from Section 3.4, we observe that the radius valley depends on stellar mass as well, the superposition of the radius valley for different stellar masses potentially smears the gap, making the radius valley appear shallower.

The degeneracy between stellar mass and metallicity is not fully resolved, hence we are unable to determine the sole effect of stellar metallicity on the radius valley in this work. We therefore consider



**Figure 16.** Distribution of host stars parameters in our work, compared with F18 and V18. The properties shown here, from the top left- to the bottom right-hand panel, are stellar radius  $R_*$ , mass  $M_*$ , *Kepler* magnitude  $K_{\text{smag}}$ , and effective temperature  $T_{\text{eff}}$ . For systems with multiple transiting planets, stars are counted multiple times.

**Table 9.** Average values of stellar properties of the host stars in the planetary sample used in this work, compared with F18 and V18.  $\bar{x}$  and  $\tilde{x}$  represent the mean and median values of the parameter  $x$ , respectively.

Sample	$\bar{R}_* (R_\odot)$	$\tilde{R}_* (R_\odot)$	$\bar{M}_* (M_\odot)$	$\tilde{M}_* (M_\odot)$	$\bar{K}_{\text{smag}}$	$\tilde{K}_{\text{smag}}$	$\bar{T}_{\text{eff}} (\text{K})$	$\tilde{T}_{\text{eff}} (\text{K})$
This work	1.08	0.99	0.98	0.95	12.27	12.31	5587	5630
F18	1.23	1.19	1.04	1.03	11.72	11.97	5788	5860
V18	1.50	1.45	1.14	1.14	11.49	11.57	5980	5952

the results related to metallicity to be inconclusive and in need of further future study.

## 5 CONCLUSION

In summary, we performed transit light curve fitting on 431 planets using *Kepler* 1-min short cadence data, the vast majority of which have not been previously analysed homogeneously using short cadence observations. In this paper, we presented their revised planetary parameters, which in some cases differ substantially from those previously reported. These differences are unrelated to stellar parameters but may be related to the details of the transit-fitting

approach or the shorter observing cadence, the effects of which should be disentangled in future studies.

By statistically analysing the small close-in planets in our sample, we observed a radius valley, which is deeper than that reported in several other studies, although not entirely empty. The valley's depth likely implies a homogeneous initial planetary core composition where the planets are similar in composition at formation, and likely to have similar iron fractions. We provide a table of those planets that appear to be inside the valley, as they may warrant further study.

The radius valley has a strong dependence on planetary orbital period and the mass of the host star. It also displays a weak dependence on the stellar age. We compared several possible radius valley models using SVMs. We determined that the radius valley can

**Table 10.** List of planets inside the radius valley as defined by this work. The coordinates (RA and Dec.) are taken from *Kepler* Q1-17 DR 25 catalogue (Thompson et al. 2018), except for K02533.03, where data are taken from *Kepler* Q1-16 catalogue (Mullally et al. 2015).

KOI	Kepler name	$P$ (d)	$t_0$ (BJD-2454833)	$R_p/R_*$	$R_p$ ( $R_\oplus$ )	RA ( $^\circ$ )	Dec. ( $^\circ$ )
K00049.01	Kepler-461 b	8.313 784 $\pm$ 0.000 015	175.9915 $\pm$ 0.0008	0.0287 $\pm$ 0.0010	4.03 $^{+0.17}_{-0.17}$	292.249 02	46.164 822
K00070.03	Kepler-20 A d	77.611 598 $\pm$ 0.000 019	164.7274 $\pm$ 0.0005	0.0263 $\pm$ 0.0003	2.52 $^{+0.07}_{-0.07}$	287.698	42.338 718
K00092.01	KOI-92.01	65.704 594 $\pm$ 0.000 018	137.4419 $\pm$ 0.0005	0.0263 $\pm$ 0.0006	3.02 $^{+0.11}_{-0.11}$	283.374 82	43.788 219
K00094.02	Kepler-89 A c	10.423 684 $\pm$ 0.000 005	138.0092 $\pm$ 0.0005	0.0266 $\pm$ 0.0006	3.97 $^{+0.13}_{-0.13}$	297.333 07	41.891 121
K00105.01	Kepler-463 b	8.981 015 $\pm$ 0.000 002	136.6493 $\pm$ 0.0005	0.0313 $\pm$ 0.0004	3.65 $^{+0.11}_{-0.10}$	298.937 04	44.857 91
K00107.01	Kepler-464 b	7.256 964 $\pm$ 0.000 011	134.0232 $\pm$ 0.0007	0.0198 $\pm$ 0.0004	3.46 $^{+0.11}_{-0.11}$	294.835 17	48.982 361
K00108.01	Kepler-103 b	15.965 333 $\pm$ 0.000 013	142.1780 $\pm$ 0.0006	0.0221 $\pm$ 0.0002	3.49 $^{+0.04}_{-0.04}$	288.984 56	40.064 529
K00111.03	Kepler-104 A d	51.755 294 $\pm$ 0.000 018	271.0894 $\pm$ 0.0005	0.0232 $\pm$ 0.0003	2.66 $^{+0.07}_{-0.07}$	287.604 61	42.166 779
K00122.01	Kepler-95 b	11.523 073 $\pm$ 0.000 005	131.9686 $\pm$ 0.0004	0.0205 $\pm$ 0.0002	3.24 $^{+0.10}_{-0.10}$	284.482 45	44.398 041
K00157.02	Kepler-11 d	22.687159 $\pm$ 0.000 014	148.4549 $\pm$ 0.0006	0.0282 $\pm$ 0.0006	3.34 $^{+0.11}_{-0.10}$	297.115 11	41.909 142
K00174.01	Kepler-482 b	56.354185 $\pm$ 0.000 019	144.8366 $\pm$ 0.0007	0.0339 $\pm$ 0.0013	2.92 $^{+0.14}_{-0.14}$	296.822 91	48.107 552
K00238.01	Kepler-123 b	17.232 309 $\pm$ 0.000 018	135.0923 $\pm$ 0.0008	0.0223 $\pm$ 0.0006	3.21 $^{+0.13}_{-0.13}$	296.998 63	42.781 96
K00285.01	Kepler-92 b	13.748 833 $\pm$ 0.000 015	179.2788 $\pm$ 0.0007	0.0198 $\pm$ 0.0003	3.71 $^{+0.06}_{-0.06}$	289.086 06	41.562 958
K00317.01	Kepler-521 b	22.208 119 $\pm$ 0.000 015	206.3592 $\pm$ 0.0006	0.0207 $\pm$ 0.0003	3.69 $^{+0.11}_{-0.11}$	298.816 38	43.998 039
K00351.03	Kepler-90 d	59.737 034 $\pm$ 0.000 020	158.9612 $\pm$ 0.0009	0.0217 $\pm$ 0.0006	2.80 $^{+0.11}_{-0.11}$	284.4335	49.305 161
K00351.04	Kepler-90 e	91.940 461 $\pm$ 0.000 020	134.2987 $\pm$ 0.0010	0.0198 $\pm$ 0.0007	2.56 $^{+0.11}_{-0.11}$	284.4335	49.305161
K00386.01	Kepler-146 b	31.158 789 $\pm$ 0.000 019	173.9038 $\pm$ 0.0009	0.0297 $\pm$ 0.0007	3.30 $^{+0.12}_{-0.12}$	294.110 75	38.710 232
K00386.02	Kepler-146 c	76.732 517 $\pm$ 0.000 020	200.6716 $\pm$ 0.0010	0.0258 $\pm$ 0.0013	2.87 $^{+0.16}_{-0.16}$	294.110 75	38.710 232
K00408.01	Kepler-150 c	7.381 981 $\pm$ 0.000 007	173.0729 $\pm$ 0.0008	0.0355 $\pm$ 0.0005	3.34 $^{+0.12}_{-0.12}$	288.2341	40.520 901
K00416.01	Kepler-152 b	18.207 957 $\pm$ 0.000 015	185.8427 $\pm$ 0.0006	0.0383 $\pm$ 0.0006	3.12 $^{+0.10}_{-0.09}$	286.865 48	41.989 079
K00435.05	Kepler-154 c	62.302 788 $\pm$ 0.000 020	179.0982 $\pm$ 0.0010	0.0266 $\pm$ 0.0010	3.04 $^{+0.15}_{-0.15}$	289.780 52	49.896 53
K00509.02	Kepler-171 c	11.463 477 $\pm$ 0.000 013	137.3859 $\pm$ 0.0008	0.0328 $\pm$ 0.0008	3.30 $^{+0.15}_{-0.14}$	296.771 91	41.755 539
K00510.04	Kepler-172 e	35.118 523 $\pm$ 0.000 020	152.1229 $\pm$ 0.0010	0.0248 $\pm$ 0.0021	2.82 $^{+0.26}_{-0.26}$	283.368 41	41.821 861
K00555.02	Kepler-598 c	86.494 779 $\pm$ 0.000 020	181.8831 $\pm$ 0.0009	0.0272 $\pm$ 0.0008	2.51 $^{+0.10}_{-0.10}$	293.123 41	40.934 769
K00665.01	Kepler-207 d	5.868 083 $\pm$ 0.000 009	170.3244 $\pm$ 0.0009	0.0202 $\pm$ 0.0004	3.69 $^{+0.11}_{-0.11}$	290.030 52	42.166 05
K00707.02	Kepler-33 f	41.028 059 $\pm$ 0.000 019	172.5788 $\pm$ 0.0009	0.0207 $\pm$ 0.0004	3.64 $^{+0.13}_{-0.13}$	289.077 55	46.005 219
K00707.03	Kepler-33 e	31.784 774 $\pm$ 0.000 020	135.8721 $\pm$ 0.0009	0.0188 $\pm$ 0.0005	3.30 $^{+0.12}_{-0.12}$	289.077 55	46.005 219
K00708.01	Kepler-216 c	17.406 653 $\pm$ 0.000 017	171.0063 $\pm$ 0.0008	0.0230 $\pm$ 0.0006	3.88 $^{+0.14}_{-0.14}$	293.728 06	46.12915
K00711.01	Kepler-218 c	44.699 505 $\pm$ 0.000 020	174.8232 $\pm$ 0.0008	0.0272 $\pm$ 0.0007	3.07 $^{+0.11}_{-0.11}$	295.412 81	46.266 472
K00800.02	Kepler-234 c	7.212 030 $\pm$ 0.000 017	172.8172 $\pm$ 0.0009	0.0283 $\pm$ 0.0012	3.61 $^{+0.28}_{-0.26}$	291.653 53	38.494 659
K00834.02	Kepler-238 d	13.233 546 $\pm$ 0.000 019	140.3211 $\pm$ 0.0010	0.0197 $\pm$ 0.0005	3.37 $^{+0.19}_{-0.18}$	287.897 13	40.637 821
K00834.05	Kepler-238 f	50.447 315 $\pm$ 0.000 020	178.4929 $\pm$ 0.0010	0.0203 $\pm$ 0.0009	3.48 $^{+0.23}_{-0.22}$	287.89713	40.637 821
K00881.01	Kepler-712 b	21.022 471 $\pm$ 0.000 017	207.6765 $\pm$ 0.0007	0.0391 $\pm$ 0.0008	3.14 $^{+0.18}_{-0.17}$	294.909 73	42.935 261
K00907.04	Kepler-251 e	99.640 965 $\pm$ 0.000 021	198.6899 $\pm$ 0.0009	0.0320 $\pm$ 0.0017	2.82 $^{+0.19}_{-0.19}$	296.566 22	44.105 862
K00921.02	Kepler-253 d	18.119 898 $\pm$ 0.000 018	182.6165 $\pm$ 0.0008	0.0346 $\pm$ 0.0011	3.01 $^{+0.16}_{-0.15}$	291.841 98	44.858 089
K00934.01	Kepler-254 b	5.826 654 $\pm$ 0.000 006	173.0110 $\pm$ 0.0009	0.0368 $\pm$ 0.0011	3.62 $^{+0.26}_{-0.24}$	288.1647	45.816 509
K00941.01	Kepler-257 c	6.581 482 $\pm$ 0.000 009	174.7876 $\pm$ 0.0009	0.0429 $\pm$ 0.0009	3.75 $^{+0.15}_{-0.15}$	297.315 98	46.023 258
K00954.02	Kepler-259 c	36.924 954 $\pm$ 0.000 019	174.2245 $\pm$ 0.0010	0.0291 $\pm$ 0.0017	2.85 $^{+0.19}_{-0.19}$	288.211 94	46.615 002
K01001.01	Kepler-264 b	40.806 846 $\pm$ 0.000 020	155.7126 $\pm$ 0.0009	0.0159 $\pm$ 0.0003	3.39 $^{+0.12}_{-0.12}$	292.044 62	37.376 24
K01198.01	Kepler-275 c	16.088 329 $\pm$ 0.000 018	139.4928 $\pm$ 0.0010	0.0232 $\pm$ 0.0011	3.55 $^{+0.31}_{-0.29}$	292.479 71	38.514 919
K01215.02	Kepler-277 c	33.006 310 $\pm$ 0.000 020	145.3914 $\pm$ 0.0010	0.0161 $\pm$ 0.0008	3.04 $^{+0.17}_{-0.17}$	286.583 16	39.077 202
K01270.01	Kepler-57 b	5.729 326 $\pm$ 0.000 005	138.5598 $\pm$ 0.0009	0.0356 $\pm$ 0.0024	3.16 $^{+0.24}_{-0.24}$	293.6413	44.657 04
K01486.02	Kepler-302 b	30.183 689 $\pm$ 0.000 018	146.6480 $\pm$ 0.0009	0.0286 $\pm$ 0.0011	3.27 $^{+0.21}_{-0.20}$	294.316 99	43.629 341
K01563.04	Kepler-305 d	16.738 655 $\pm$ 0.000 019	359.4178 $\pm$ 0.0009	0.0338 $\pm$ 0.0022	2.84 $^{+0.22}_{-0.22}$	299.224 33	40.343182
K01598.01	Kepler-310 c	56.476 167 $\pm$ 0.000 019	143.8052 $\pm$ 0.0008	0.0301 $\pm$ 0.0007	2.75 $^{+0.10}_{-0.10}$	288.839 36	46.986 74
K02051.01	Kepler-355 c	25.762 459 $\pm$ 0.000 020	147.7050 $\pm$ 0.0009	0.0230 $\pm$ 0.0010	2.95 $^{+0.18}_{-0.17}$	285.799 47	42.811 779
K02390.01	Kepler-1219 b	16.104 672 $\pm$ 0.000 020	135.0156 $\pm$ 0.0010	0.0120 $\pm$ 0.0011	3.51 $^{+0.46}_{-0.46}$	297.215 79	47.378 521
K02414.02	Kepler-384 c	45.348 527 $\pm$ 0.000 020	142.2527 $\pm$ 0.0010	0.0157 $\pm$ 0.0012	2.78 $^{+0.22}_{-0.22}$	286.026 12	44.782 871
K02533.03	KOI-2533.03	26.115 290 $\pm$ 0.000 019	145.5642 $\pm$ 0.0010	0.0122 $\pm$ 0.0011	4.01 $^{+0.38}_{-0.38}$	286.715 64	48.645 279
K02639.01	KOI-2639.01	25.108 060 $\pm$ 0.000 020	146.4407 $\pm$ 0.0010	0.0191 $\pm$ 0.0083	3.69 $^{+1.63}_{-1.62}$	285.365 17	49.201 561

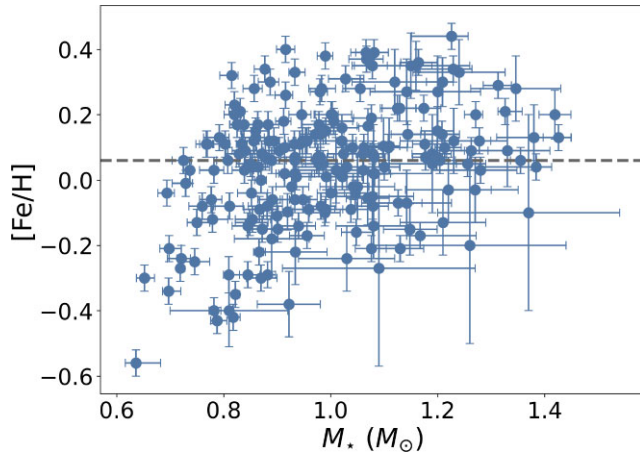


**Figure 17.** Metallicity and mass of the host stars are used in this work. The grey-dotted line  $[\text{Fe}/\text{H}] = 0.06$  shows the cut-off between stars of low and high metallicity as defined in this work. We note a lack of stars with low metallicity and large stellar mass.

best be described in four dimensions using the formula

$$R_{p,\text{valley}} \propto P^A M_*^B (\text{age})^C \quad (20)$$

with  $A = -0.096_{-0.027}^{+0.023}$ ,  $B = 0.231_{-0.064}^{+0.053}$ , and  $C = 0.033_{-0.025}^{+0.017}$ .

Comparing our radius valley dependencies with theoretical models, we found that in  $R_p$ - $S$ - $M_*$  space, our posterior distributions are most consistent with core-powered mass-loss, where they agree within less than  $1\sigma$ . The models are also consistent with photoevaporation scenarios at  $\approx 2\sigma$ . We did not find a significant dependence of the radius valley on stellar metallicity.

With the Transiting Exoplanet Survey Satellite (e.g. Ricker et al. 2015) now in its extended mission, and the upcoming launch of the PLANetary Transits and Oscillations of stars mission (e.g. Rauer et al. 2014), such future planetary studies could drastically increase the number of planets with radii measurements and hence provide an even more detailed view of the radius valley. This work highlights the impact of careful transit fitting using short, 1-min cadence observations to obtain precise planetary radii. This will likely be of key importance to derive precise planetary radii using transit observations from ongoing and future missions, which will ultimately allow us to better understand the formation and evolution of small close-in planets.

## ACKNOWLEDGEMENTS

This paper includes data collected by the Kepler mission and obtained from the MAST data archive at the Space Telescope Science Institute (STScI). Funding for the Kepler mission is provided by the NASA Science Mission Directorate. STScI is operated by the Association of Universities for Research in Astronomy, Inc., under NASA contract NAS 5-26555. CSKH would like to thank the Science and Technology Facilities Council (STFC) for funding support through a PhD studentship. We would like to thank Erik Petigura, James Rogers, and James Owen for insightful discussions. We also thank the anonymous reviewer for taking their time to review the paper, and for their valuable suggestions, which have improved the manuscript.

## DATA AVAILABILITY

The *Kepler* 1-min short cadence light curves are available for download on the NASA MAST database<sup>1</sup>, at [doi:10.17909/T98304](https://doi.org/10.17909/T98304). The parameter estimates from HMC posteriors are provided in the Appendix tables.

## REFERENCES

- Astropy Collaboration et al., 2013, *A&A*, 558, A33 (V18)  
 Astropy Collaboration et al., 2018, *AJ*, 156, 123  
 Berger T. A., Huber D., Gaidos E., van Saders J. L., Weiss L. M., 2020, *AJ*, 160, 108  
 Bourque M. et al., 2021, The Exoplanet Characterization Toolkit (ExoCTK), Zenodo  
 Claret A., Bloemen S., 2011, *A&A*, 529, A75  
 Cloutier R., Menou K., 2020, *AJ*, 159, 211  
 David T. J. et al., 2021, *AJ*, 161, 265  
 Foreman-Mackey D. et al., 2021, *J. Open Source Softw.*, 6, 3285  
 Fulton B. J. et al., 2017, *AJ*, 154, 109  
 Fulton B. J., Petigura E. A., 2018, *AJ*, 156, 264 (F18)  
 Furlan E. et al., 2017, *AJ*, 153, 71  
 Ginsburg A. et al., 2019, *AJ*, 157, 98  
 Ginzburg S., Schlichting H. E., Sari R., 2016, *ApJ*, 825, 29  
 Ginzburg S., Schlichting H. E., Sari R., 2018, *MNRAS*, 476, 759  
 Gupta A., Schlichting H. E., 2019, *MNRAS*, 487, 24  
 Gupta A., Schlichting H. E., 2020, *MNRAS*, 493, 792  
 Holczer T. et al., 2016, *ApJS*, 225, 9  
 Huber D. et al., 2013, *ApJ*, 767, 127  
 Kipping D. M., 2013, *MNRAS*, 435, 2152  
 Lee E. J., Chiang E., 2016, *ApJ*, 817, 90  
 Lee E. J., Chiang E., Ormel C. W., 2014, *ApJ*, 797, 95  
 Lightcurve Collaboration et al., 2018, Astrophysics Source Code Library, record ascl:1812.013.  
 Lopez E. D., Fortney J. J., 2013, *ApJ*, 776, 2  
 Lopez E. D., Rice K., 2018, *MNRAS*, 479, 5303  
 Loyd R. O. P., Shkolnik E. L., Schneider A. C., Richey-Yowell T., Barman T. S., Peacock S., Pagano I., 2020, *ApJ*, 890, 23  
 Lundkvist M. S. et al., 2016, *Nature Commun.*, 7, 11201  
 Luque R., Pallé E., 2022, *Science*, 377, 1211  
 MacDonald M. G., 2019, *MNRAS*, 487, 5062  
 Martinez C. F., Cunha K., Ghezzi L., Smith V. V., 2019, *ApJ*, 875, 29  
 Mathur S. et al., 2017, *ApJS*, 229, 30  
 Mordasini C., 2020, *A&A*, 638, A52  
 Mullally F. et al., 2015, *ApJS*, 217, 31  
 Owen J. E., Adams F. C., 2019, *MNRAS*, 490, 15  
 Owen J. E., Murray-Clay R., 2018, *MNRAS*, 480, 2206  
 Owen J. E., Wu Y., 2013, *ApJ*, 775, 105  
 Owen J. E., Wu Y., 2017, *ApJ*, 847, 29  
 Petigura E. A. et al., 2017, *AJ*, 154, 107  
 Petigura E. A. et al., 2022, *AJ*, 163, 179  
 Petigura E. A., 2020, *AJ*, 160, 89  
 Raghavan D. et al., 2010, *ApJS*, 190, 1  
 Rasmussen C. E., Williams C. K. I., 2006, Gaussian Processes for Machine Learning. The MIT Press, Cambridge, MA  
 Rauer H. et al., 2014, *Exp. Astron.*, 38, 249  
 Ricker G. R. et al., 2015, *J. Astron. Telesc. Instrum. Syst.*, 1, 014003  
 Rogers J. G., Owen J. E., 2021, *MNRAS*, 503, 1526  
 Rogers J. G., Gupta A., Owen J. E., Schlichting H. E., 2021, *MNRAS*, 508, 5886  
 Rowe J. F. et al., 2014, *ApJ*, 784, 45  
 Salvatier J., Wiecki T. V., Fonnesbeck C., 2016, *PeerJ Comput. Sci.*, 2, e55

<sup>1</sup><https://archive.stsci.edu>



Silva Aguirre V. et al., 2015, *MNRAS*, 452, 2127  
 Smith J. C. et al., 2012, *Publ. Astron. Soc. Pac.*, 124, 1000  
 Stumpe M. C. et al., 2012, *Publ. Astron. Soc. Pac.*, 124, 985  
 Thompson S. E. et al., 2018, *ApJS*, 235, 38  
 Van Eylen V. et al., 2019, *AJ*, 157, 61  
 Van Eylen V. et al., 2021, *MNRAS*, 507, 2154  
 Van Eylen V., Albrecht S., 2015, *ApJ*, 808, 126  
 Van Eylen V., Agentoft C., Lundkvist M. S., Kjeldsen H., Owen J. E., Fulton B. J., Petigura E., Snellen I., 2018, *MNRAS*, 479, 4786

## SUPPORTING INFORMATION

Supplementary data are available at [MNRAS](https://www.mnras.org) online.

[H22\\_table1\\_full.txt](#)

[H22\\_tableA1\\_full.txt](#)

[H22\\_tableA2\\_full.txt](#)

[H22\\_tableA3\\_full.txt](#)

Please note: Oxford University Press is not responsible for the content or functionality of any supporting materials supplied by the authors. Any queries (other than missing material) should be directed to the corresponding author for the article.

## APPENDIX A: EXTRA MATERIAL

**Table A1.** Host star parameters of planets fitted in this work.  $R_*$ ,  $M_*$ ,  $T_{\text{eff}}$ ,  $[\text{Fe}/\text{H}]$ , and  $K_{\text{smag}}$  are taken from the following sources: 1: F18, 2: V18. Stellar ages are taken from F18. Radius correction factors (RCFs) are taken from Furlan et al. (2017); we take  $\text{RCF} = 1.0000$  where there are no measurements in Furlan et al. (2017).  $\rho_*$ ,  $u_0$ , and  $u_1$  are resulting parameters from the transit fitting. Only the first 10 host stars are shown here; the full table is available online in a machine-readable format.

KOI	$R_*$ ( $R_{\odot}$ ) (1)	$M_*$ ( $M_{\odot}$ ) (1)	$T_{\text{eff}}$ (K) (1)	$[\text{Fe}/\text{H}]$ (dex) (1)	$K_{\text{smag}}$ (1)	$R_*$ ( $R_{\odot}$ ) (2)	$M_*$ ( $M_{\odot}$ ) (2)	$T_{\text{eff}}$ (K) (2)	$[\text{Fe}/\text{H}]$ (dex) (2)	$K_{\text{smag}}$ (2)	Age (Gyr)	RCF	$\rho_*$ ( $\text{g cm}^{-3}$ )	$u_0$	$u_1$
41	$1.53^{+0.03}_{-0.03}$	$1.10^{+0.07}_{-0.03}$	$5854^{+60}_{-60}$	$0.10 \pm 0.04$	$9.768$	$1.51^{+0.01}_{-0.01}$	$1.11^{+0.02}_{-0.02}$	$5903^{+53}_{-66}$	$0.10 \pm 0.09$	$11.197$	$6.92^{+1.91}_{-0.80}$	1.0083	$0.313 \pm 0.015$	$0.46 \pm 0.08$	$0.17 \pm 0.11$
46	$1.66^{+0.05}_{-0.04}$	$1.24^{+0.03}_{-0.09}$	$5661^{+60}_{-60}$	$0.39 \pm 0.04$	$12.011$	N/A	N/A	N/A	N/A	N/A	$5.25^{+0.73}_{-1.69}$	1.0000	$0.279 \pm 0.025$	$0.52 \pm 0.18$	$0.27 \pm 0.16$
49	$1.29^{+0.03}_{-0.03}$	$0.95^{+0.03}_{-0.03}$	$5779^{+60}_{-60}$	$-0.06 \pm 0.04$	$11.917$	N/A	N/A	N/A	N/A	N/A	$10.47^{+1.21}_{-1.12}$	1.0000	$0.441 \pm 0.021$	$0.34 \pm 0.12$	$0.25 \pm 0.13$
69	$0.94^{+0.02}_{-0.02}$	$0.87^{+0.03}_{-0.03}$	$5594^{+60}_{-60}$	$-0.09 \pm 0.04$	$8.37$	$0.91^{+0.02}_{-0.02}$	$0.89^{+0.07}_{-0.07}$	$5669^{+75}_{-75}$	$-0.18 \pm 0.10$	$9.931$	$9.12^{+2.94}_{-2.10}$	1.0000	$1.044 \pm 0.055$	$0.44 \pm 0.04$	$0.16 \pm 0.06$
70	$0.88^{+0.02}_{-0.02}$	$0.94^{+0.02}_{-0.02}$	$5508^{+60}_{-60}$	$0.11 \pm 0.04$	$10.871$	N/A	N/A	N/A	N/A	N/A	$3.09^{+1.99}_{-1.57}$	1.0054	$1.391 \pm 0.052$	$0.45 \pm 0.04$	$0.24 \pm 0.07$
72	$1.08^{+0.03}_{-0.03}$	$0.87^{+0.02}_{-0.01}$	$5599^{+60}_{-60}$	$-0.11 \pm 0.04$	$9.496$	$1.07^{+0.01}_{-0.01}$	$0.92^{+0.01}_{-0.02}$	$5678^{+55}_{-49}$	$-0.10 \pm 0.06$	$10.961$	$12.88^{+1.48}_{-0.89}$	1.0005	$0.690 \pm 0.019$	$0.38 \pm 0.10$	$0.24 \pm 0.13$
82	$0.72^{+0.02}_{-0.02}$	$0.80^{+0.01}_{-0.02}$	$4909^{+60}_{-60}$	$0.11 \pm 0.04$	$9.351$	N/A	N/A	N/A	N/A	N/A	$1.07^{+0.89}_{-1.58}$	1.0000	$2.039 \pm 0.055$	$0.62 \pm 0.06$	$0.09 \pm 0.07$
85	$1.44^{+0.03}_{-0.03}$	$1.25^{+0.01}_{-0.03}$	$6220^{+60}_{-60}$	$0.13 \pm 0.04$	$9.806$	$1.40^{+0.01}_{-0.01}$	$1.20^{+0.03}_{-0.03}$	$6193^{+43}_{-52}$	$0.15 \pm 0.08$	$11.018$	$2.95^{+0.34}_{-0.41}$	1.0001	$0.428 \pm 0.019$	$0.33 \pm 0.06$	$0.25 \pm 0.07$
92	$1.06^{+0.02}_{-0.02}$	$1.08^{+0.03}_{-0.03}$	$5923^{+60}_{-60}$	$0.09 \pm 0.04$	$10.3$	$1.05^{+0.03}_{-0.03}$	$1.08^{+0.11}_{-0.11}$	$5952^{+19}_{-19}$	$0.02 \pm 0.15$	$11.667$	$2.34^{+1.35}_{-1.40}$	1.0000	$0.894 \pm 0.049$	$0.41 \pm 0.12$	$0.26 \pm 0.13$
94	$1.37^{+0.03}_{-0.03}$	$1.18^{+0.03}_{-0.02}$	$18181^{+60}_{-60}$	$0.07 \pm 0.04$	$10.926$	N/A	N/A	N/A	N/A	N/A	$3.47^{+0.64}_{-0.56}$	1.0000	$0.462 \pm 0.021$	$0.33 \pm 0.11$	$0.37 \pm 0.16$

**Table A2.** Planetary parameters from transit fits performed in this work.  $P$ ,  $t_0$ ,  $R_p/R_*$ ,  $b$ ,  $e$ , and  $\omega$  are obtained directly from fitting,  $a/R_*$  and  $S$  are indirectly calculated. The  $R_p/R_*$  values from 1: F18 and 2: V18 are also included for comparison. Only the first 10 planets are shown here; the full table is available online in a machine-readable format.

KOI	Kepler name	$P$ (d)	$t_0$ (BJD-2454833)	$R_p/R_*$	$R_p/R_*$ (1)	$R_p/R_*$ (2)	$b$	$e$	$\omega$ ( $^\circ$ )	$a/R_*$	$S$ ( $\delta_{\text{gp}}$ )
K00041.01	Kepler-100 c	$12.815893 \pm 0.000008$	$122.9476 \pm 0.0005$	$0.0138 \pm 0.0002$	$0.0140^{+0.0001}_{-0.0006}$	$0.0134^{+0.0001}_{-0.0001}$	$0.39 \pm 0.13$	$0.06 \pm 0.04$	$30 \pm 96$	$14.36 \pm 1.20$	$245.37 \pm 20.59$
K00041.02	Kepler-100 b	$6.887062 \pm 0.000007$	$133.1781 \pm 0.0008$	$0.0082 \pm 0.0001$	$0.0081^{+0.0013}_{-0.0002}$	$0.0079^{+0.0004}_{-0.0002}$	$0.63 \pm 0.05$	$0.05 \pm 0.04$	$3 \pm 107$	$9.26 \pm 0.88$	$590.40 \pm 56.33$
K00041.03	Kepler-100 d	$35.333093 \pm 0.000019$	$153.9835 \pm 0.0009$	$0.0104 \pm 0.0002$	$0.0092^{+0.0023}_{-0.0003}$	$0.0092^{+0.0004}_{-0.0002}$	$0.81 \pm 0.02$	$0.05 \pm 0.04$	$1 \pm 104$	$27.50 \pm 2.51$	$66.87 \pm 6.13$
K00046.02	Kepler-101 c	$6.029792 \pm 0.000020$	$132.4816 \pm 0.0010$	$0.0073 \pm 0.0007$	$0.0069^{+0.0005}_{-0.0005}$	N/A	$0.41 \pm 0.21$	$0.05 \pm 0.04$	$-0 \pm 103$	$8.13 \pm 0.77$	$646.80 \pm 61.97$
K00049.01	Kepler-461 b	$8.313784 \pm 0.000015$	$175.9915 \pm 0.0008$	$0.0287 \pm 0.0010$	$0.0259^{+0.0003}_{-0.0003}$	N/A	$0.75 \pm 0.11$	$0.23 \pm 0.13$	$77 \pm 77$	$14.75 \pm 2.22$	$213.71 \pm 32.30$
K00069.01	Kepler-93 b	$4.726739 \pm 0.000001$	$134.9265 \pm 0.0001$	$0.0151 \pm 0.0001$	$0.0159^{+0.0002}_{-0.0008}$	$0.0149^{+0.0001}_{-0.0001}$	$0.23 \pm 0.13$	$0.20 \pm 0.09$	$105 \pm 58$	$13.06 \pm 1.39$	$252.14 \pm 27.04$
K00070.01	Kepler-20 A c	$10.854089 \pm 0.000003$	$138.6082 \pm 0.0002$	$0.0290 \pm 0.0002$	$0.0300^{+0.0018}_{-0.0006}$	N/A	$0.18 \pm 0.11$	$0.09 \pm 0.03$	$86 \pm 39$	$22.49 \pm 0.80$	$75.81 \pm 2.80$
K00070.02	Kepler-20 A b	$3.696115 \pm 0.000001$	$134.5021 \pm 0.0002$	$0.0182 \pm 0.0002$	$0.0209^{+0.0014}_{-0.0023}$	N/A	$0.49 \pm 0.08$	$0.05 \pm 0.04$	$26 \pm 101$	$10.24 \pm 0.83$	$365.46 \pm 29.71$
K00070.03	Kepler-20 A d	$77.611598 \pm 0.000019$	$164.7274 \pm 0.0005$	$0.0263 \pm 0.0003$	$0.0259^{+0.0005}_{-0.0003}$	N/A	$0.36 \pm 0.13$	$0.06 \pm 0.04$	$33 \pm 96$	$78.67 \pm 6.41$	$6.20 \pm 0.51$
K00070.05	Kepler-20 A f	$19.577627 \pm 0.000020$	$135.2063 \pm 0.0009$	$0.0091 \pm 0.0004$	$0.0098^{+0.0004}_{-0.0003}$	N/A	$0.65 \pm 0.06$	$0.05 \pm 0.04$	$7 \pm 104$	$30.66 \pm 2.84$	$40.78 \pm 3.81$
...	...	...	...	...	...	...	...	...	...	...	...

**Table A3.** Transit jitter and GP parameters from transit fitting of planetary systems in this work. Only the first 10 systems are shown here; the full table is available online in a machine-readable format.

KOI	$\log \sigma_{\text{lc}}$	$\log \sigma_{\text{gp}}$	$\log \rho_{\text{gp}}$
41	$-8.4379 \pm 0.0016$	$-9.5822 \pm 0.0105$	$-4.5121 \pm 0.0335$
46	$-7.1119 \pm 0.0037$	$-9.1794 \pm 0.1025$	$-4.3449 \pm 0.2492$
49	$-7.3268 \pm 0.0044$	$-8.8595 \pm 0.0680$	$-1.2568 \pm 0.1547$
69	$-8.9861 \pm 0.0019$	$-10.1248 \pm 0.0133$	$-4.8968 \pm 0.0382$
70	$-7.7689 \pm 0.0012$	$-9.4665 \pm 0.0150$	$-3.7110 \pm 0.0415$
72	$-8.4175 \pm 0.0053$	$-9.6473 \pm 0.0392$	$-4.0440 \pm 0.1139$
82	$-8.1671 \pm 0.0018$	$-8.6193 \pm 0.0116$	$-3.2278 \pm 0.0240$
85	$0.0000 \pm 0.0000$	$0.0000 \pm 0.0000$	$0.0000 \pm 0.0000$
92	$-8.1505 \pm 0.0062$	$-9.8036 \pm 0.0880$	$-3.9919 \pm 0.2448$
94	$-7.8819 \pm 0.0017$	$-9.8028 \pm 0.0308$	$-2.9898 \pm 0.1183$
...	...	...	...

This paper has been typeset from a  $\text{\LaTeX}$  file prepared by the author.